Interspecific variation in the limb long bones among modern rhinos - extent and drivers

Christophe Mallet [Corresp., 1], **Raphaël Cornette** [2], **Guillaume Billet** [3], **Alexandra Houssaye** [1]

[1] Mécanismes adaptatifs et évolution (MECADEV), UMR 7179, MNHN, CNRS, Museum national d'Histoire naturelle, Paris, France

[2] Institut de Systématique, Evolution, Biodiversité (ISYEB), UMR 7205, MNHN, CNRS, SU, EPHE, UA, Museum national d'Histoire naturelle, Paris, France

[3] Centre de Recherche en Paléontologie - Paris (CR2P), UMR CNRS 7207, MNHN, CNRS, SU, Museum national d'Histoire naturelle, Paris, France

Corresponding Author: Christophe Mallet
Email address: christophe.mallet@edu.mnhn.fr

Among amniotes, numerous lineages are subject to a convergent evolutionary trend towards body mass and size increases. Terrestrial large species may face important constraints linked to weight bearing, and the limb segments are particularly affected by such constraints, because of their role in body support and locomotion. Such groups showing important limb modifications related to body mass have been called “graviportal”. Often considered graviportal, rhinos are among the heaviest terrestrial mammals and are thus of particular interest to understand the limb modifications related to body mass and size increase. Here, we propose a morphofunctional study of the shape variation of the limb long bones among the five living rhinos to understand how the shape may vary between these species in relation with body size, body mass and phylogeny. We used 3D geometric morphometrics and comparative analyses to quantify the shape variation. Our results indicate that the five species display important morphological differences pending on the considered bones. The humerus and the femur exhibit noticeable interspecific differences between African and Asiatic rhinos, associated to an important impact of the body mass. The radius and ulna are more strongly correlated with body mass. While the tibia exhibits shape variation both linked with phylogeny and body mass, the fibula displays the maximal intraspecific variation, questioning its functional role and the origin of these morphological changes. We highlight three distinct morphotypes on bone shape, which appear in accordance with the phylogeny. The influence of body mass also appears unequally expressed on the different bones. Body mass increase among the five extant species is marked by an increase of the general robustness, a reinforcement of the main lever arms for muscles, and a development of medial parts of the bones. Our study indicates that the bone morphology is affected differently by body mass and size increases pending on the considered bones and species. It also underlines that the morphological features linked to body mass increase are not similar between rhinos and other heavy

mammals such as elephants and hippos, suggesting that the weight bearing constraint can lead to different morphological responses.

Interspecific variation in the limb long bones among modern rhinos - extent and drivers

Christophe Mallet[1], Raphaël Cornette[2], Guillaume Billet[3], Alexandra Houssaye[1]

[1] Mécanismes adaptatifs et évolution (MECADEV), UMR 7179, MNHN, CNRS, 55 rue Buffon, CP 55, 75005, Paris, France

[2] Institut de Systématique, Evolution, Biodiversité (ISYEB), UMR 7205, MNHN, CNRS, SU, EPHE, UA, 57 rue Cuvier, CP 50, 75005 Paris, France

[3] Centre de Recherche en Paléontologie - Paris (CR2P), UMR CNRS 7207, MNHN, CNRS, SU, 8 rue Buffon, CP 38, 75005 Paris, France

Corresponding author:

Christophe Mallet

55 rue Buffon, CP 55, 75005, Paris, France

Email address: christophe.mallet@edu.mnhn.fr

Abstract

Among amniotes, numerous lineages are subject to a convergent evolutionary trend towards body mass and size increases. Terrestrial large species may face important constraints linked to weight bearing, and the limb segments are particularly affected by such constraints, because of their role in body support and locomotion. Such groups showing important limb modifications related to body mass have been called “graviportal”. Often considered graviportal, rhinos are among the heaviest terrestrial mammals and are thus of particular interest to understand the limb modifications related to body mass and size increase. Here, we propose a morphofunctional study of the shape variation of the limb long bones among the five living rhinos to understand how the shape may vary between these species in relation with body size, body mass and phylogeny. We used 3D geometric morphometrics and comparative analyses to quantify the shape variation. Our results indicate that the five species display important morphological differences pending on the considered bones. The humerus and the femur exhibit noticeable interspecific differences between African and Asiatic rhinos, associated to an important impact of the body mass. The radius and ulna are more strongly correlated with body mass. While the tibia exhibits shape variation both linked with phylogeny and body mass, the fibula displays the maximal intraspecific variation, questioning its functional role and the origin of these morphological changes. We highlight three distinct morphotypes on bone shape, which appear in accordance with the phylogeny. The influence of body mass also appears unequally expressed on the different bones. Body mass increase among the five extant species is marked by an increase of the general robustness, a reinforcement of the main lever arms for muscles, and a development of medial parts of the bones. Our study indicates that the bone morphology is affected differently by body mass and size increases pending on the considered bones and species. It also underlines that the morphological features linked to body mass increase are not similar between rhinos and other heavy mammals such as elephants and hippos, suggesting that the weight bearing constraint can lead to different morphological responses.

Keywords

rhinoceros; limb bones; 3D geometric morphometrics; morphofunctional anatomy; body mass; body size; graviportality.

44

Introduction

Many vertebrate lineages present a convergent evolutionary trend towards a body mass increase through time (Depéret, 1907; Raia et al., 2012; Baker et al., 2015; Bokma et al., 2016). Size and mass augmentation implies metabolic and musculoskeletal modifications for the whole body to bear its own weight (McMahon, 1973). One of the most noticeable body changes related to weight bearing concern modifications of the appendicular skeleton; animals displaying such adaptive traits are said to be “graviportal” (Hildebrand, 1974). This concept introduced by Gregory (1912) and Osborn (1929) has been defined based on both anatomical and locomotion aspects: the commonly accepted criteria are, in addition to a body mass of several hundreds of kilograms, columnar limbs with a stylopodium lengthening and an autopodium shortening, robust bones, large feet with enlarged adipose cushions, reduced phalanges, long strides associated with the inability to gallop (Gregory, 1912; Osborn, 1929; Coombs, 1978). This condition was opposed to the “cursorial” one characterizing light and running animals (e.g. horses and many ungulates). Between these two extremes, intermediate categories tended to sharpen this tentative locomotor classification, with “subcursorial” for moderate cursorial adaptations with good running performances (e.g. felids and canids), and “mediportal” for animals with conformations meeting both the weight bearing aspect and running capacities (e.g. suids, tapirs) (Gregory, 1912; Coombs, 1978; Eisenmann & Guérin, 1984). These categories remain massively used in functional morphology and locomotion studies (e.g. Maynard Smith & Savage, 1956; Coombs, 1978; Eisenmann & Guérin, 1984; Prothero et al., 1986; Biewener, 1989a; Stein & Casinos, 1997; Polly, 2007; Scherler et al., 2013; MacLaren & Nauwelaerts, 2016). Hildebrand (1974) proposed an arbitrary body mass of 900 kg beyond which the species is considered as graviportal, but without justification for this threshold. Carrano (1999) tackled this problem by replacing these discrete categories by a multivariate continuum of locomotor habits ranging from graviportal to cursorial based on bone and muscular insertion measurements, chosen to be “biomechanically relevant” but performed only on the femur, tibia and third metatarsal.

As a consequence, the categorization of some taxa as graviportal may vary depending on authors. Among living mammals, elephants, rhinos and hippos are commonly considered as the three main graviportal taxa (Alexander & Pond, 1992). Elephants obviously fulfil all the

morphological and biomechanical criteria defining graviportality (Coombs, 1978; Langman et al., 1995). However, hippo's peculiar morphology (barrel-like body and shortened limbs) linked to semi-aquatic habits has been considered alternately as mediportal (Coombs, 1978; Ross, 1984) or graviportal (Alexander & Pond, 1992; Carrano, 1999; MacFadden, 2005; Stilson, Hopkins & Davis, 2016). Rhino's graviportal condition is surely the less consensual: Gregory (1912) and Osborn (1929) considered rhinos as mediportal whereas later works assigned them a graviportal condition (Prothero and Sereno, 1982; Eisenmann and Guérin, 1984). Becker (2003) and Becker et al. (2009) dug onto this question and developed a "gracility index" based on the work of Guérin (1980) to categorize modern and fossil rhinos, but only based on third metacarpal and metatarsal proportions. The use of this index sharpened the classification of modern rhinos distinguishing mediportal and graviportal forms (Table 1).

Regardless of the locomotor type to which they belong, the family Rhinocerotidae includes ones of the heaviest land mammal species after elephants, displaying adaptations to sustain their high body mass (Alexander & Pond, 1992). The five remaining modern rhino species exhibit an important variation in body mass and size (Table 1), ranging from less than a ton for *Dicerorhinus sumatrensis* to more than 3 tons for the biggest known specimens of *Ceratotherium simum*. They are all good walkers and runners, able to gallop and reach a max speed of 55 km/h (Dinerstein, 2011). However, important ecological differences also exist (Groves, 1967a,b, 1972; Groves & Kurt, 1972; Laurie, Lang & Groves, 1983; Hillman-Smith & Groves, 1994; Dinerstein, 2011; Groves & Leslie, 2011): the three Asiatic rhinos are excellent swimmers and very familiar with a water environment whereas the two African ones are easily stopped by a relatively deep river. While *Ceratotherium simum* is a pure grazer, *Rhinoceros unicornis* can both graze and browse small shrubs, leafy material and fruits, the three other species being mainly leaf browsers. Before the drastic decrease of their natural habitats under human pressure, rhinos occupied a wide geographic range across Africa and Asia (Dinerstein, 2011; Rookmaaker & Antoine, 2013). Moreover, the fossil record of the superfamily Rhinocerotoidea contains many lineages displaying evolutionary convergence towards an increase of body mass (Prothero & Schoch, 1989; Prothero, 1998; Antoine, 2002; Becker, 2003; Scherler et al., 2013). However, despite the importance of rhino species to understand evolution towards high body mass and the fact that they are ones of the heaviest surviving land mammals, only a few studies really explored the variation of their limb bone morphology in relation to their body proportions. After

the pioneering works of Cuvier (1812) and de Blainville & Nicard (1839) describing the postcranial anatomy of modern rhinos, almost no work tried to broadly analyse and compare the morphology of their limb bones. Guérin (1980) proposed a substantial comparative anatomy work on the whole skeleton of the five extant species. This study aimed to emphasize determination criteria with a direct application to fossil forms. Despite considerations on inter- and intraspecific osteological variations on modern rhinos, this work did not fully explore the patterns of shape variation in this group. Furthermore, most of the previous studies used a classic morphometric approach with linear measurements on bones, an approach which cannot precisely take into consideration the whole shape of the bone in 3D. To our knowledge, no morphofunctional analyses have been carried out on limb long bones of modern rhinos taking into consideration their whole shape.

Here we propose to explore the variation in the shape of the limb long bones among the five modern rhino species using a 3D geometric morphometrics approach. We describe interspecific patterns of morphological variation for the six bones composing the stylopodium and the zeugopodium, taking into account the intraspecific variation. We also explore the potential links of shape patterns with body size and phylogenetic relations between species.

Material and Methods

Sample

We selected 62 dry skeletons in different European museums belonging to the five extant rhino species: *Ceratotherium simum* Burchell, 1817; *Dicerorhinus sumatrensis* Fischer, 1814; *Diceros bicornis* Linnaeus, 1758; *Rhinoceros sondaicus* Desmarest, 1822 and *Rhinoceros unicornis* Linnaeus, 1758 (Table 2). We followed the taxonomic attribution given by each institution for most of the specimens, except for three individuals determined or reattributed by ourselves on osteological criteria and later confirmed by our morphometric analysis (see Table 2). As some skeletons were incomplete, we studied altogether 53 humeri, 49 radii, 46 ulnae, 56 femora, 52 tibiae and 50 fibulae. We kept only mature specimens with fully fused epiphyses (adults) or displaying a majority of fused epiphyses (subadults). Bones showing breakages or unnatural deformations were not considered in our analysis. In accordance with the observations of Guérin (1980), we did not notice any major difference between captive and wild animals, neither

through visual and osteological observations nor in our morphometric analyses: we therefore did not take into account this parameter. Sexual dimorphism occurs among rhinos but has been mostly investigated regarding the external morphology of the animals (Dinerstein, 1991, 2011; Berger, 1994; Zschokke & Baur, 2002). The few studies that have explored the osteological variations between sexes indicated only slight absolute metric divergences depending on species (Guérin, 1980; Groves, 1982). This suggests that intraspecific variation due to sex may be marginal when compared to interspecific variation, and probably more related to the size of the bone than to the shape. Furthermore, since almost half of our sample lacked sex information and that we had twice more males than females, we could not carefully address gender in our study (see Results).

3D models

Bones were mostly digitized with a structured-light three-dimensional scanner (Artec Eva) and reconstructed with the Artec Studio Professional software (v12.1.1.12 – Artec 3D, 2018). Complementarily, 19 bones were digitized with a photogrammetric approach, following Mallison & Wings (2014) and Fau, Cornette & Houssaye (2016). Sets of photos were taken all around the bones and aligned to reconstruct a 3D model with the Agisoft Photoscan software (v1.4.2 – Agisoft, 2018). Previous studies indicated no significant difference between 3D models obtained with these two methods (Petti et al., 2008; Remondino et al., 2010; Fau, Cornette & Houssaye, 2016). Five bones were digitized using medical computed tomography scanners at the Royal Veterinary College, London (Equine Hospital) and at the University of California, San Francisco (Department of Radiology & Biomedical Imaging). Bone surfaces were extracted as meshes using the Avizo software (v9.5.0 – Thermo Fisher Scientific, 2018). Each mesh was decimated to reach 250,000 vertices and 500,000 faces using MeshLab (v2016.12 - Cignoni et al., 2008). We mainly selected left bones during acquisition: when this was impossible, right bones were selected and then mirrored before analysis.

Anatomical terminology

All anatomical terms used to describe bones were borrowed to classic references: the *Nomina Anatomica Veterinaria* (World Association of Veterinary Anatomists & International Committee on Veterinary Gross Anatomical Nomenclature, 2005) and anglicized terms of Barone (2010a)

for general osteology and bone orientation, Guérin (1980) for precise rhino anatomy, completed by the contributions of Colyn (1980), Antoine (2002) and Heissig (2012). Despite these previous works, one anatomical feature remained unnamed, leading us to use our own designation: we called “palmar process” the process facing the coronoid process on the palmar border of the radius proximal epiphysis. Muscle insertions were described after the general anatomy of horses (Barone, 2010b), completed by the work of Beddard & Treves (1889) and some complementary information from Guérin (1980) on rhino myology and Fisher, Scott & Naples (2007) and Fisher, Scott & Adrian (2010) on hippo’s.

Geometric Morphometrics

To analyse shape variation in our sample, we performed 3D geometric morphometrics, a widely used approach allowing to quantify morphological differences between objects using landmark coordinates (Adams, Rohlf & Slice, 2004; Zelditch et al., 2012).

Landmark digitization

Following the procedure described by Gunz, Mitteroecker & Bookstein (2005), Gunz & Mitteroecker (2013) and Botton-Divet et al. (2016), we defined the bones’ shape using anatomical landmarks and curve and surface sliding semi-landmarks. Each curve is bordered by anatomical landmarks as recommended by Gunz & Mitteroecker (2013). We placed all landmarks and curves using the IDAV Landmark software (v3.0 – Wiley et al., 2005). We used 35 anatomical landmarks on the humerus, 23 on the radius, 21 on the ulna, 27 on the femur, 24 on the tibia and 12 on the fibula. Details of landmark numbers and locations used for each bone are given in Supplemental Data S1.

Following the procedure detailed by Botton-Divet et al. (2016), we created a template to place surface semi-landmarks for each bone: a specimen was randomly chosen on which all anatomical landmarks, curve and surface sliding semi-landmarks were placed. We then used this template for the projection of surface sliding semi-landmarks on the surface of the other specimens. Projection was followed by a relaxation step to ensure that projected points matched the actual surface of the meshes. Curve and surface sliding semi-landmarks were then slid to minimize the bending energy of a Thin Plate Sline between each specimen and the template at first, and then two times between the result of the preceding step and the Procrustes consensus of the complete

dataset. Therefore, all landmarks can be treated at the end as anatomical landmarks and analysed with classic procedure as Procustes Analysis (see below). Projection, relaxation and sliding processes were conducted using the Morpho package in the R environment (R Core Team, 2014). Details of the process are provided in the documentation of the package (Schlager, 2018).

Repeatability tests

For each bone, we tested the repeatability of the anatomical landmark digitization taking measurements ten times on three specimens of the same species, *Ceratotherium simum*, chosen to display the closest morphology and size. We superimposed these measurements using a Generalized Procrustes Analysis and visualized the results using a Principal Component Analysis (PCA). Results showed a variation within specimens clearly smaller than the variation between specimens (see Supplemental Fig. S2) and allowed us to consider our anatomical landmarks as relevant to describe shape variation.

Generalized Procrustes Analyses

After the sliding step, we performed Generalized Procrustes Analyses (GPA) (Gower, 1975; Rohlf & Slice, 1990) to remove the effects of size and of the relative position of the points and to isolate only the shape information. As our dataset contained more variables than observations, we used a Principal Component Analysis (PCA) to reduce dimensionality as preconized by Gunz & Mitteroecker (2013) and visualize the specimen repartition in the morphospace. We computed theoretical consensus shape of our sample and used it to calculate a TPS deformation of the template mesh. We then used this newly created consensus mesh to compute theoretical shapes associated with the maximum and minimum of both sides of each PCA, as well as mean shapes of each bone for each species. GPA, PCA and shape computations were done using the "Morpho" and "geomorph" packages (Adams & Otárola-Castillo, 2013; Adams, Collyer & Kaliontzopoulou, 2018; Schlager, 2018) in the R environment (R Core Team, 2014). Neighbour Joining method was used to construct trees displaying relative Euclidian distances between individuals based on all principal component scores obtained with the PCA, allowing a global visualisation of the relationships between all the specimens. Trees were computed with the "ape" package (Paradis et al., 2018).

Allometry effect

We tested the effect of allometry, defined as "the size-related changes of morphological traits" (Klingenberg, 2016). Pearson's correlation tests were performed to look for correlation between the principal components and the centroid size (log_{10}) for each bone. We also used the function *procD.allometry* of the "geomorph" package to perform a Procrustes ANOVA (a linear regression model using Procrustes distances between species instead of covariance matrices – see Goodall, 1991) to quantify the shape variation related to the centroid size, and to visualize theoretical shapes associated to minimal and maximal sizes of our sample (Adams & Otárola-Castillo, 2013; Adams, Collyer & Kaliontzopoulou, 2018). This test was performed taking into account group affiliation (e.g. species) to highlight respective roles of centroid size and species determination on the shape variation. In the absence of individual body mass for the majority of our sample, we also performed a Procrustes ANOVA with the cube root of the mean mass attributed to each species (Table 1), each species being associated to the mean mass of its species. As for the centroid size, theoretical shapes associated to minimal and maximal mean mass were computed. Plots of the linear regressions of shape scores against log-transformed centroid size were also computed.

Results

Shape analysis

We describe here the results of our PCA for each bone and focus on the theoretical shape variations along the two main axes. For each bone, we chose to represent relevant views and anatomical features. Complete visualizations of the different theoretical shapes for the two first axes are available in Supplemental Data S3. Analysis of shape relations among our sample is completed by the Neighbour Joining trees provided in Supplemental Figure S4.

Humerus

The first two axes of the PCA computed on the humerus represent 60.6% of the total variance (Fig. 1A). The first axis represents more than half of the global variance (53%) and the five species appear clearly sorted along it, opposing *D. sumatrensis* on the positive side to *C. simum*

on the negative one, i.e. the lightest and heaviest species, respectively. *D. bicornis* is grouped with *C. simum* on the negative part of the axis, whereas *R. sondaicus* is on the positive part. *R. unicornis* occupies the centre of the axis, between *D. bicornis* and *R. sondaicus*. Points repartition in the morphospace and Neighbour Joining trees indicate a clear separation between African and Asiatic rhinos (Fig. S4A). The theoretical shape at the PC1 minimum (Fig. 1B, D, F, H) displays a massive morphology, with broad both medio-laterally and cranio-caudally epiphyses and shaft; a wide humeral head, very little overhanging the diaphysis in the caudal direction; a lesser tubercle paradoxically more strongly developed than the greater tubercle, with an intermediate tubercle separating a widely open bicipital groove into unequal parts, the lateral one being the largest; a lesser tubercle convexity medially extended whereas the greater tubercle one is quite reduced in this direction; a broad and diamond-shaped *m. infraspinatus* imprint on the lateral side; a broad deltoid tuberosity not extending beyond the lateral border of the bone; a shaft with its maximal width situated between the head neck and the deltoid tuberosity; a distinct but very smooth and flat *m. teres major* tuberosity; a distal epiphysis very large because of the development of the lateral epicondyle; a smooth epicondylar crest; a medial epicondyle medio-laterally wide and cranio-caudally compressed; shallow and proximo-distally compressed olecranon fossa and trochlea, a wide trochlea displaying a main axis tilted in the dorso-ventral direction; a capitulum with a small surface area. At the opposite, the theoretical shape at the PC1 maximum (Fig. 1C, E, G, I) shows a slender and thin aspect; a more rounded humeral head overhanging caudally the diaphysis; a greater tubercle more strongly developed than the lesser one and extending medially, conferring a more closed aspect to the bicipital groove, where the intermediate tubercle is almost absent; a slightly marked lesser tubercle convexity whereas the greater tubercle one is massive; a rounded and reduced *m. infraspinatus* insertion; a deltoid tuberosity strongly protruding laterally; a straight and thin shaft; no visible *m. teres major* tuberosity; a narrow distal epiphysis, with a small development of the lateral epicondyle; a sharp epicondylar crest; ; a medial epicondyle cranio-caudally developed and overhanging the olecranon fossa; a deep and wide olecranon fossa; a far less compressed trochlea, with an axis less dorso-ventrally tilted; and an almost completely absent capitulum.

Along the second axis (7.6%), we observe this time that *C. simum* and *D. sumatrensis* are grouped together on the negative part of the axis, with the three other species on the positive part, whereas they are opposed along the first axis. This second axis expresses the separation

between the lightest and the heaviest rhino species on the one hand and the three other species on the other hand. The theoretical shape at the PC2 minimum displays a humeral head stretched in the caudal direction; a lesser tubercle more developed than the greater one, delimiting a W-shaped bicipital groove; a distal epiphysis proximo-distally extended, with an epicondylar crest starting almost on the middle of the shaft; a rounded and wide olecranon fossa. At the opposite, the theoretical shape at the PC2 maximum shows a rounded humeral head; a strong development of both tubercles and a more closed bicipital groove; a distal epiphysis medio-laterally stretched, with the epicondylar crest starting at the distal third of the shaft; an olecranon fossa proximo-distally compressed and more rectangular; and a well-developed lateral epicondyle.

Radius

The first two axes of the PCA performed on the radius express 52.3% of the total variance (Fig. 2A). The first axis (36.4%) opposes *D. sumatrensis* and *D. bicornis* to *R. unicornis* and *C. simum*. *R. sondaicus* overlaps both *R. unicornis* and *D. bicornis* clusters. Point dispersion along this axis indicates an important intraspecific variation for *D. sumatrensis*, and to a lesser extent for *D. bicornis* and *R. sondaicus*. Unlike for the humerus, phylogenetically related species are not grouped together on PCA and Neighbour Joining trees (Fig. S4B). The theoretical shape at the PC1 minimum (Fig. 2B, D, F, H) displays a massive morphology with large shaft and epiphyses; an asymmetrical proximal articular surface (constituting the ulnar notch), with a medial portion twice as large as the lateral one; a protruding lateral insertion relief whereas the radial tuberosity is little prominent; a lateral synovial articulation surface for the ulna medio-laterally reduced; a rectangular and thin medial synovial articulation surface for the ulna; a triangular proximal articular surface for the ulna as wide medio-laterally as proximo-distally; a thick shaft with an interosseous space opening close to the proximal epiphysis: consequently, the interosseous crest runs along the diaphysis to the distal articular surface for the ulna; a broad distal epiphysis in the medio-lateral direction, with a strong medial tubercle developed on the dorsal face; a distal articular surface compressed in the dorso-ventral direction; an articular surface for the scaphoid little extended proximally; a trapezoid and wide articular surface for the semilunar; a well-developed radial styloid process. The theoretical shape at the PC1 maximum (Fig. 2C, E, G, I) displays a more slender morphology; a proximal articular surface less asymmetrical despite the development of the medial part; an almost absent lateral insertion

relief; a completely flat radial tuberosity; a lateral synovial articulation for the ulna medio-laterally stretched; a rectangular and thin medial synovial articulation for the ulna; a triangular proximal articular surface for the ulna, medio-laterally short and proximo-distally stretched; a thin and slender shaft, with an interosseous space opening at the proximal third of the total length; a poorly visible interosseous crest; a distal epiphysis far less dorso-ventrally compressed and a lateral tubercle on the dorsal side poorly developed; a distal articular surface dorso-ventrally wide with the surface responding to the scaphoid extending proximally; a trapezoid and reduced articular surface for the semilunar; a less developed radial styloid process with a rounded border.

The second axis (15.9%) discriminates mainly *R. sondaicus* from the four other species. *R. unicornis* displays little extension along this axis; neither does *D. bicornis*, only driven on the negative side by a single individual. *R. unicornis*'s extension along the second axis is very limited, contrary to *C. simum*'s and *D. sumatrensis*'s. The theoretical shape at the PC2 minimum displays a slender morphology, with a strongly asymmetrical proximal articular surface; a palmar process opposed to the coronoid process proximally reduced; a distal epiphysis dorso-ventrally broad, with a developed lateral prominence; a little developed radial styloid process; an articular surface for the scaphoid proximally extended. The theoretical shape at PC2 maximum displays a more massive shape; a deeper and more symmetrical proximal articular surface with a well-developed palmar process; a dorso-ventrally compressed distal epiphysis with a more developed styloid process.

Ulna

The first two axes of the PCA performed on the ulna express 41.5% of the total variance (Fig. 3A). The first axis (22.1%) separates *D. sumatrensis* and *D. bicornis* on the positive part and *R. sondaicus*, *R. unicornis* and *C. simum* on the negative part. However, *C. simum*'s and *R. unicornis*'s clusters overlap along this axis. The general pattern on both PCA and Neighbour Joining trees is close to the one observed for the radius (Fig. S4C). The theoretical shape at the PC1 minimum (Fig. 3B, D, F, H) displays a thick morphology with large epiphyses; a massive olecranon tuberosity with a medial tubercle – where inserts the medial head of the *m. triceps brachii* – oriented dorsally; an anconeus process poorly developed dorsally and medio-laterally wide, as is the articular surface constituting the trochlear notch (receiving the humeral trochlea);

a medially stretched medial part of the articular surface for the humerus; a short interosseous crest ending at the shaft half, with the interosseous space; a broad shaft with a triangular section; a straight palmar border whereas the shaft is medially curved; a massive distal epiphysis with a wide insertion surface for the radius; an articular surface for the triquetrum medio-laterally wide and little concave, while the one responding to the pisiform is crescent-shaped and little extended proximally. The theoretical shape for the PC1 maximum (Fig. 3C, E, G, I) displays a more gracile morphology; a slender olecranon tuberosity with a medial tubercle where inserts the medial head of the *m. triceps brachii* oriented in the palmar direction; an anconeus process dorsally developed and medio-laterally narrow, as is the articular surface of the trochlear notch; a slightly medially stretched medial part of the articular surface; a sharp interosseous crest; a thin and straight shaft; a distal epiphysis medio-laterally compressed and little concave; an articular surface for the triquetrum medio-laterally narrow; a triangular and proximally well-developed articular surface for the pisiform.

The second axis (19.4%) separates quite clearly the three Asian species from the African ones. The theoretical shape at the PC2 minimum displays a slender and straight morphology with a high square-shaped olecranon process, medio-laterally flattened, more stretched in the palmar direction; a wide and squared anconeus process; a straight and regular shaft; a distal epiphysis medio-laterally compressed with a concave articular surface for the triquetrum and a distally developed styloid process; a proximally extended articular facet for the pisiform. The theoretical shape at the PC2 maximum displays a more massive and medially concave shape with an olecranon process medio-laterally inflated and rounded in the palmar direction; an anconeus process little developed dorsally and laterally tilted; an articular surface constituting the trochlear notch proximo-distally compressed and extending medially; a medio-laterally wide articular surface for the triquetrum; a little developed styloid process; an articular surface for the pisiform poorly extended proximally and square-shaped.

Femur

The first two axes of the PCA performed on the femur express 45.0% of the global variance (Fig. 4A). The first principal component (36.1%) clearly separates the heaviest and lightest rhino species, with *D. sumatrensis* on the positive part and *C. simum* on the negative part. *D. bicornis*'s, *R. sondaicus*'s and *R. unicornis*'s clusters overlap on the negative part of the axis. *D.*

bicornis and *R. unicornis* specimens partly overlap *C. simum* cluster too. The isolation of *D. sumatrensis* drives the clusters organization along the first axis. The general pattern observed on the Neighbour Joining tree is closer to the humerus one, with African and Asiatic species grouped together, respectively (Fig. S4D). The theoretical shape at the PC1 minimum (Fig. 4B, D, F, H) displays a massive morphology with large epiphyses and a curved medial border, conferring a concave aspect to the diaphysis axis; a large femoral head, off-centred relatively to the shaft main axis, supported by a very large neck; a small and shallow *fovea capitis* oriented medio-caudally; a greater trochanter convexity expending strongly latero-distally; the absence of trochanteric notch between the convexity and the top of the trochanter (Fig. 4F); a proximo-distally reduced trochanteric fossa; a sharp lesser trochanter running along the medial edge, which is cranio-caudally flattened below the humeral head; a third trochanter extending strongly laterally, cranially and proximally towards the greater trochanter convexity, and much curved towards the medial direction; a quite irregular shaft section along the bone – flattened below the proximal epiphysis and more trapezoid towards the distal epiphysis; a broad distal epiphysis with developed medial and lateral epicondyles; a shallow supracondylar fossa; a wide trochlea, with a main rotation axis aligned with the shaft axis; a large and cranially expended medial lip of the trochlea separated from the lateral one by a deep trochlear groove; a medial condyle surface area larger than the lateral condyle one, both being separated by a narrow intercondylar space. At the opposite, the theoretical shape at the PC1 maximum (Fig. 4C, E, G, I) is more slender with a straight and regular shaft; a rounded femoral head aligned with the shaft main axis and supported by at thinner neck; a more pronounced and rounded *fovea capitis* oriented almost completely caudally; a greater trochanter convexity little developed latero-distally; a more pronounced trochanter top despite the absence of trochanteric notch; a thin lesser trochanter situated on the caudal border of the medial side; a rounded third trochanter more developed laterally than cranially; a quite regular and trapezoid shaft section; a distal epiphysis medio-laterally broader and oriented medially; an almost absent supracondylar fossa; a less developed trochlear medial lip separated from the lateral one by a shallow trochlear groove; a lateral condyle more oblique and divergent relatively to the medial one, increasing the intercondylar space; symmetrical medial and lateral condylar surfaces.

The second axis (8.9%) clearly opposes *D. sumatrensis, C. simum* and *D. bicornis* on the positive part to the two *Rhinoceros* species on the negative part, *D. sumatrensis*'s cluster being driven

towards negative values by a single individual. The theoretical shape at the PC2 minimum is mainly characterized by a flattened femoral head with a strong neck; a rounded and large *fovea capitis* oriented medio-caudally; a greater trochanter convexity latero-distally expended; a long and thin lesser trochanter; an extremely developed third trochanter in lateral, cranial and proximal directions; a straight and regular shaft; a broad distal epiphysis with important development of both epicondyles; a trochlea rotation axis aligned with the main axis of the shaft. The theoretical shape at the PC2 maximum displays a more rounded head, with a more stretched neck; no *fovea capitis* at all but a little groove on the head border; a greater trochanter convexity little expanded latero-distally; a short and more medially developed lesser trochanter; a rounded third trochanter little developed in cranial and proximal directions; a straight shaft; a distal epiphysis less medio-laterally broad; a narrower intercondylar space; a more inflated medial condyle.

Tibia

The first two axes of the PCA performed on the tibia express 50.0% of the global variance (Fig. 5A). The first axis (29.1%) separates roughly *D. bicornis* and *D. sumatrensis* on the positive part and *C. simum, R. sondaicus* and *R. unicornis* on the negative part. *D. bicornis* and shows an important intraspecific variation along both axes. Neighbour Joining tree structure is less clear than for previous bones: both *Rhinoceros* species isolate from most of the other specimens, *C. simum* appears also separated from *D. bicornis* and *D. sumatrensis*. However, one *C. simum* and three *D. sumatrensis* specimens are closer from the *Rhinoceros* group than from their own respective species (Fig. S4E). The theoretical shape at the PC1 minimum (Fig. 5B, D, F, H) displays a massive morphology with broad shaft and epiphyses, both in cranio-caudal and medio-lateral directions; medial and lateral intercondylar tubercles having the same height and a reduced central intercondylar area; a broad cranial intercondylar area; a medial articular surface larger than the lateral one, with the sliding surface for the *m. popliteus* tendon extending caudally; a U-shaped popliteal notch; a rounded tibial tuberosity, laterally deflected and medially bordered by a shallow groove; a shallow extensor groove; a regularly triangular proximal articular surface for the fibula extending distally; a thick tibial crest disappearing at the middle of the shaft, where the bone section is the smallest; a distal epiphysis medio-laterally broad and rectangular in section; a distal articular surface for the fibula reduced in height and triangular-

shaped, surmounted by a smooth interosseous crest running towards the middle of the shaft; a distal articular surface for the talus roughly rectangular, with a lateral groove larger and shallower than the medial one, separated by a prominent intermediate process without synovial fossa; an articular surface with a rotation axis aligned with the bone main axis; a prominent medial malleolus. The theoretical shape at the PC1 maximum (Fig. 5C, E, G, I) displays a slender morphology with a thin shaft; a lateral intercondylar tubercle more proximally extended than the medial one and a relatively large central intercondylar area; a lateral condylar surface extending cranially, reducing the cranial intercondylar area; medial and lateral articular roughly equal surface areas; a V-shaped popliteal notch; a tibial tuberosity slightly more laterally deflected; a deeper tuberosity groove; a nail-shaped proximal articular surface for the fibula; a sharper tibial crest disappearing just before the first half of the shaft; a distal epiphysis more compressed cranio-caudally; a distal articular surface for the fibula displaying a large triangle synostosis area occupying a third of the shaft and prolonged by a sharp interosseous crest. There is no major difference in the distal articular shape between PC1 maximum and minimum, except that the caudal apophysis is less prominent in the distal direction.

The second axis (20.9%) clearly separates the two African species (*C. simum* and *D. bicornis*) on the positive part from the three Asian species (*D. sumatrensis, R. sondaicus* and *R. unicornis*) on the negative part. The theoretical shape at the PC2 minimum displays a slightly more slender morphology; a proximal plateau higher cranially than caudally and forming a closer angle with the diaphysis axis; a high intercondylar eminence; a lateral articular surface more caudally extended than the medial one; a tibial tuberosity well separated from the condyles by deep tuberosity and extensor grooves; a straight shaft ending with divergent borders forming a large and rectangular distal epiphysis; a distal articular surface for the fibula forming a regular triangle surmounted by a sharp interosseous crest; a medially extended medial malleolus, resulting in a rectangular articular surface with the talus, where the medial groove is narrow and deep, occupying a third of the area, whereas the lateral groove is shallow and broad. The theoretical shape at the PC2 maximum displays a more massive morphology, with a cranio-caudal inflation of the epiphyses; a proximal plateau almost perpendicular to the diaphysis axis; a lower intercondylar eminence; a lateral condyle surface almost twice less large than the medial one, which is more developed caudally; a massive tibial tuberosity strongly deviated laterally, delimited by very shallow tuberosity and extensor grooves and resulting in a very large cranial

intercondylar area; a straight shaft ending with almost parallel medial and lateral borders and a square-shaped distal epiphysis; a medial malleolus less medially deflated; a squared distal articular surface for the talus with medial and lateral grooves showing similar surface area and depth.

Fibula

The first two axes of the PCA performed on the fibula express 55.9% of the global variance (Fig. 6). Contrary to the five previous analyses, the first axis (40.7%) here seems particularly driven by a strong intraspecific variation. *C. simum*'s and *D. sumatrensis*'s clusters are stretched along the PC1 and overlap with almost every other specimens. *D. bicornis*'s cluster is quite stretched along the axis too and only the two *Rhinoceros* species display less intraspecific variation. This pattern does not seem linked to sex, age class or condition (wild or captive): despite the presence of slightly more females and subadults on the negative part of the component, we did not consider this observation as robust enough to state on this question. Consequently, we chose to display and analyse the specimen repartition along the second and third components instead. Theoretical shapes associated to the PC1 are available in Supplemental Data S3.

PC2 and PC3 express 22.9% of the global variance (Fig. 7A). The second component (15.2%) opposes *C. simum* on the negative side to *D. sumatrensis* on the positive side, whereas *D. bicornis*'s, *R. sondaicus*'s and *R. unicornis*'s clusters have a more central disposition. As for the tibia, the Neighbour Joining tree structure appears less clearly sorted by species than for other bones. If *Rhinoceros* species group together and African ones as well, *D. sumatrensis*'s sample is split in two subgroups mixed with *R. unicornis* and African rhinos respectively (Fig. S4F). The theoretical shape at the PC2 minimum (Fig. 7B, D, F, H, J) displays a broad morphology with large epiphyses and a straight shaft; a rounded head with a proximal articular surface for the tibia cranio-medially oriented; a head width similar to the shaft one; a robust shaft with two strong cranio-lateral and caudo-lateral lines running down the distal epiphysis and enlarging cranio-caudally towards the distal epiphysis; a sharp and irregular interosseous crest; a distal epiphysis medio-laterally compressed with little development of the two distal tubercles at the end of the lateral crests; a shallow lateral groove; a triangular distal articular surface for the tibia, occupying only the last distal quarter of the bone length; a short and ovoid articular surface for the talus with a sharp distal ridge. The theoretical shape at the PC2 maximum (Fig. 7C, E, G, I, K)

displays a slender morphology with a strongly curved shaft; a medio-laterally flat head extending cranio-caudally and overhanging strongly the diaphysis; a thin shaft with two sharp lateral crests running along it: these crests end with two developed tubercles surrounding a deep lateral groove; a distal articular surface for the tibia extending from the distal third of the shape and forming a stretched triangle; a wider and kidney-shaped articular surface for the talus, forming two distal tips responding to the two lateral tubercles: between them on the distal face, a large groove is visible, ending at the centre of the face.

The third component (7.7%) mainly opposes *D. bicornis* on the positive part to *R. sondaicus* on the negative part. However, this opposition is mainly driven by a small number of individuals (two for *D. bicornis* and four for *R. sondaicus*) and the majority of the other individuals overlap. The theoretical shape at the PC3 minimum shows a massive morphology, with broad shaft and epiphyses; a cranio-caudally broad head, overhanging the shaft laterally; a proximal articular surface for the tibia oriented almost completely medially; a straight shaft displaying a constant width along the bone; cranio-lateral and caudo-lateral crests running almost parallel towards the distal end of the bone, forming two developed tubercles surrounding a deep groove; an interosseous space covered by irregular reliefs and bordered by a sharp interosseous crest; a distal articular surface for the tibia forming a triangle cranially deported; a kidney-shaped distal articular surface for the talus, with a distal border separated from the lateral tubercles by a groove stopping at the middle of the distal face. The theoretical shape at the PC3 maximum shows an extremely thin morphology with a flattened and poorly developed head; a proximal articular surface oriented almost completely in the cranial direction; a torsion of almost 90 degrees between the orientation of the proximal and distal articular surfaces for the tibia; a very thin and flat shaft; cranio-lateral and caudo-lateral crests running along the diaphysis ending on the distal epiphysis with few developed tubercles; a distal articular surface for the tibia forming a slender triangle; a relatively small distal articular surface for the talus, with a less pronounced kidney-shape; a groove on the distal face medio-laterally compressed.

Interspecific morphological variation

In addition to global interspecific patterns of shape, we shortly describe the main morphological features characterizing each species. Mean shapes of each bone for the five species are available in Supplemental Data S5.

Limb long bones of *C. simum* present a general massive and robust aspect. The humerus is thick and shows a strong development of the lesser tubercle and the lateral epicondyle, as well as a proximal broadening in the cranio-caudal direction. The radius and ulna are robust and display an important medial development of the articular parts constituting the trochlear notch. The ulna bears a strong olecranon tubercle. The distal articular surface for the carpals constituted by the two bones is medio-laterally wide and compressed in the cranio-caudal direction. The hind limb bones are robust as well, this robustness being mainly expressed in the medio-lateral direction for the femur. This bone displays a rounded and thick head, strong greater and third trochanters, and a distal trochlea laterally oriented. The tibia and fibula are robust as well, with a wide tibial plateau supporting the knee articulation and a squared distal articulation for the talus.

For *D. bicornis*, the general aspect of the humerus is close to the one observed on *C. simum*, particularly for the epiphyses (e.g. the shape of the bicipital groove, the development of the lesser tubercle and of the lateral epicondyle), though its degree of robustness is less intense. The radius is relatively slender but the proximal articular surface displays a cranial border with a marked groove under the coronoid process, also observed on *C. simum*. The ulna is slender as well with a thin olecranon process and limited medial development. Both distal epiphyses form a medio-laterally wide articular surface for the carpals, poorly cranio-caudally compressed. As for hind limb bones, the femur is only slightly robust, with poorly developed trochanters and a slender diaphysis. Tibia and fibula are less thick too, with a squared articular surface for the talus as well. *D. bicornis* displays noticeable morphological similarities with *C. simum*.

The bone general morphology is very similar between both *R. sondaicus* and *R. unicornis*, being often more robust in *R. sondaicus.* For these two species, the humerus displays an important development of both lesser and greater tubercles, resulting in an asymmetrical bicipital groove. *R. sondaicus*'s greater tubercle is even sometimes higher than the lesser one, which is not the case for *R. unicornis*. The distal epiphysis is wide but with a medial epicondyle less developed than in *C. simum* and *D. bicornis*, and a rectangular olecranon fossa. The radius exhibits medio-laterally large epiphyses and a quite robust diaphysis, with a proximal articular surface similar in both *Rhinoceros* species, with a straight cranial border unlike in African rhinos. The distal epiphysis is rectangular and cranio-caudally compressed. *R. unicornis* distinguishes from *R. sondaicus* in having a more robust radius, with a more asymmetrical proximal epiphysis, a

551 deeper radial tuberosity and a larger distal articular surface. The ulna is also very similar, the one
552 of *R. unicornis* being slightly more robust. The general aspect remains extremely close, with a
553 developed olecranon, a medial development of the articular surface constituting the trochlear
554 notch and a quite wide distal articular surface. On the hind limb, the femur appears different, the
555 *R. unicornis*'s ones showing important development of the greater and third trochanters,
556 sometimes fused by a bony bridge as previously stated by Guérin (1980). The femur of *R.*
557 *sondaicus* appears slightly less robust, and the greater and third trochanters are less developed
558 and never fused. On the tibia, the proximal plateau is as wide as for the African taxa but the tibial
559 tuberosity is more detached from the condyles by deep tuberosity and extensor grooves. The
560 diaphysis is relatively thick and the distal articular surface is clearly rectangular. The fibula is
561 very similar as well in the two species, with a distal epiphysis curved in the caudal direction and
562 a kidney-shaped articular surface for the talus.

563 *D. sumatrensis* clearly differs from the other species. Despite clear rhinocerotid features, limb
564 long bones display unique morphological traits, with a more pronounced slenderness. On the
565 humerus, the development of the greater tubercle results in a more closed and asymmetrical
566 bicipital groove. The distal epiphysis is medio-laterally narrow with a straight trochlea axis. The
567 thin radius possesses a proximal articular surface almost symmetrical despite a medial glenoid
568 cavity slightly more developed. The ulna is thin as well, and forms with the radius a rectangular
569 articular surface for the carpals. The femur shows a high and rounded head and a poorly
570 developed third trochanter. The distal trochlea axis is more medially oriented. On the tibia, the
571 plateau is far less wide than in other species and the distal articular surface for the talus is
572 rectangular. The thin fibula displays a large head caudally bordered by a thin crest and the
573 diaphysis is strongly curved medially towards the tibia. The kidney-shape of the distal articular
574 surface for the talus resembles the *Rhinoceros* ones.

575 **Correlation with the centroid size**

576 Table 3 provides the results of the Pearson's correlation tests between the centroid size and the
577 two first principal components for each bone (and the third component for the fibula). There is a
578 significant correlation in each case between the first component and the centroid size, with
579 higher correlation coefficient values for the radius and ulna, and smaller values for the humerus
580 and fibula. The second principal component is also significantly correlated with the centroid size

for the humerus, femur and fibula, with smaller correlation coefficient values than for PC1, except for the humerus.

Allometry

Table 4 and Table 5 provide the main anatomical differences observed between theoretical shapes associated with minimal and maximal centroid size for the forelimb and hind limb bones respectively. Theoretical shapes associated with minimal and maximal centroid size are provided in Supplementary Figures S6. In the case of the fibula, we found a pattern very close to the one observed along the second axis of the PCA. Replacing the log centroid size by the cube root of the mean mass of each species results in almost identical theoretical shapes for each bone (Fig. 8 and Figure S7), only distinguishable by smooth details: towards body mass maximum, the radius and ulna appear slightly more robust than for centroid size maximum (Fig. 8D, F); the greater and third trochanters of the femur are slightly less developed towards each other (Fig. 8H). Theoretical shapes associated to minimum and maximum of centroid size are slightly more massive than the ones obtained with the body mass for the humerus, the tibia and the fibula. All theoretical shapes associated with minimal and maximal mean mass are provided in Supplementary Figures S7.

Table 6 and Table 7 provide the results of the two Procrustes ANOVAs performed on shape data, where the centroid size and the cube root of the mean body mass were respectively the independent variable. Centroid size is significantly correlated with shape for the six bones, with a determination coefficient varying between 0.10 for the fibula and 0.18 for the ulna. In every case, the correlation coefficient is higher for species than for centroid size, indicating a more important influence of the group affiliation than of the allometry. This is especially the case for the humerus, with a determination coefficient of 0.53 for the species affiliation and of only 0.13 for the centroid size. Mean body mass is also significantly correlated with shape for the six bones, with slightly higher determination coefficient values than those obtained with the centroid size. The humerus, the radius and the femur display the highest coefficients, between 0.33 and 0.26. These higher values may be due to the use of a same mean body mass for each rhino species instead of individual mass. Group affiliation could not be used in this case because of the mean body mass redundancy.

Linear regressions of shape scores against log-transformed centroid size (Fig. 9) show that *D. sumatrensis* has the smallest centroid size and is well separated from the other rhino species in most cases, except for the tibia and fibula. *R. unicornis* possesses the highest centroid size in most of the cases, except for the radius and ulna, where it shares similar centroid size values and shape scores as *C. simum*. Different tendencies can be observed: for the humerus, Asiatic rhinos have lower shape scores than African ones for a given size. Radius and ulna data display a point pattern similar to each other, with the isolation of *D. sumatrensis* towards low values, a second cluster formed by *D. bicornis* and *R. sondaicus* at average values, and a third cluster with *C. simum* and *R. unicornis* showing the highest values. This separation in three groups can be observed at a lesser extent for the femur, where *D. bicornis* and *R. sondaicus* share almost the same centroid size and shape score variations, whereas *C. simum* and *R. unicornis* are separated by their respective centroid size despite similar shape scores. Finally, tibia and fibula display rather similar patterns with an important intraspecific shape variation for some species like *D. sumatrensis* and *D. bicornis*. There is a more important continuity between the different clusters for the tibia and the fibula than for other bones, where clusters are more separated from each other.

Discussion

Identification of morphotypes and phylogenetic influence

Morphological variation isolates each rhino species from the others, more or less clearly depending on the bone considered. The observed morphological variation reflects the phylogenetic relationships between the five extant rhinos. The shape analysis of the six bones enables to clearly isolate three general bone morphotypes: the African morphotype grouping *C. simum* and *D. bicornis*, the *Rhinoceros* morphotype grouping the two *Rhinoceros* species, and the *D. sumatrensis* morphotype.

Despite the fact that we could not test the phylogenetic signal in our data because of the small number of studied species (Adams, 2014), our observations tend to indicate an impact of the phylogenetic relations. It is accepted that the two African rhino *C. simum* and *D. bicornis* are closely related (Tougard et al., 2001): they may both belong to the same subfamily – called Dicerotinae (Guérin, 1982; Gaudry, 2017) or Rhinocerotinae (Antoine, 2002; Becker, Antoine &

Maridet, 2013), pending on the authors. The two species composing the genus *Rhinoceros* are also closely related (Tougard et al., 2001), the bones of *R. unicornis* and *R. sondaicus* having sometimes been confused with each other (Groves & Leslie, 2011). Conversely, the phylogenetic position of *D. sumatrensis* remains non-consensual (Willerslev et al., 2009; Gaudry, 2017), this species being considered alternately as sister taxon of the two African species (Antoine, Duranthon & Welcomme, 2003; Cappellini et al., 2018), of the two *Rhinoceros* species (Tougard et al., 2001; Welker et al., 2017) or of all four other rhino species (Fernando et al., 2006; Piras et al., 2010). Our analyses reveal different relationship patterns, with *D. sumatrensis* more closely resembling African species for some bones (radius, ulna and tibia) and Asiatic ones for the others (humerus, femur and fibula).

Some anatomical features seem strongly influenced by phylogenetic relationships, among which some have previously been used as characters for cladistics analyses (Prothero, Manning & Hanson, 1986; Cerdeño, 1995; Antoine, 2002). On the humerus, the bicipital groove allows the sliding of a large *m. biceps brachii*, a forearm flexor playing an important locomotor role in coordinating the scapula and arm movements (Watson & Wilson, 2007; Barone, 2010b). This groove appears more closed by the greater tubercle for Asiatic rhinos, allocating less space for *m. biceps brachii* contractions. Although most analyses (Prothero, Manning & Hanson, 1986; Antoine, 2002) have coded a few characters related to the tubercles of the humerus, the complexity of the shape of this bone proximal epiphysis remains generally underestimated in phylogenetic reconstructions. Moreover, the case of the greater tubercle development observed on the humerus of Asiatic species, and mainly for *D. sumatrensis*, is of particular interest, as its functional implications are not clear (see Supplemental Data S5). *D. sumatrensis* displays the slenderest humerus of all modern rhinos, with morphological traits close to tapirs' and horses' (MacLaren & Nauwelaerts, 2016). The proximal epiphysis of *D. sumatrensis* resembles the tapirs' one, regarded by some authors as a plesiomorphic condition among Perissodactyla (Hermanson & MacFadden, 1992). This particular shape may thus represent an evolutionary heritage and it is unclear whether and how functional constraints may have also affected this shape. The greater tubercle being also an insertion area for the *m. supraspinatus*, extension movements thus seem achieved differently between African and Asiatic rhinos. The lever arm is medially stronger for *C. simum* and *D. bicornis*, and distributed both medially and laterally for *Rhinoceros* species and *D. sumatrensis*. On the distal epiphysis, characters related to the shape of

the olecranon fossa have been used in phylogenies (Heissig, 1972; Antoine, 2002). Our results confirm that the shape and depth of this fossa do not seem directly linked to the general bone robustness as observed in these studies. Moreover, this fossa is proximo-distally larger for the genus *Rhinoceros* than for *Ceratotherium* and *Diceros*.

The role of shoulder joint remains crucial in weight bearing and locomotion, and its shape may be influenced by several factors. The development of a massive greater tubercle is encountered among hippos (Fisher, Scott & Naples, 2007) and may be interpreted as a direct link with semi-aquatic habits and displacements into muddy swamps or riverbanks. This particular morphology is yet also encountered among domestic bovids for example (Barone, 2010a), which are not semi-aquatic, and, at the opposite, extinct Amynodontidae, presumed to have been semi-aquatic Oligocene rhinos (Averianov et al., 2017), did not display this greater tubercle development (Scott & Jepsen, 1941).

On the femur, the *fovea capitis* is extremely reduced in *C. simum* and absent in *D. bicornis*, whereas it is well developed in Asiatic rhinos, especially in *R. sondaicus*, confirming previous observations (Guérin, 1980; Antoine, 2002). This *fovea* provides an attachment for the accessory ligament and the femoral head ligament (Hermanson & Macfadden, 1996), acting as a hip stabilizer. The absence or reduction of *fovea capitis* in African species may be both associated to their phylogenetic proximity. This *fovea* is indeed present in many fossil rhinos (Antoine, 2002), regardless of the ecological preferences of these species. The shapes of the greater and of the third trochanters, also seem driven more by the phylogeny than by functional constraints, endorsing their use in phylogenies (Cerdeño, 1995; Antoine, 2002). On the distal epiphysis, the medial lip is more developed and inflated in all rhinos than in horses: this feature has been previously interpreted as associated to “locking” the knee joint during long standing periods in equids (Hermanson & Macfadden, 1996). But no evidence of such “knee-locking” mechanism exists among rhinos. Other authors saw in the development of this medial lip an adaptation to a more important degree of cursoriality, linked to the openness of the habitat (Janis et al., 2012). But tapirs, yet able to gallop (Sanborn & Watkins, 1950), do not display such an enlargement of the medial lip of the trochlea (Holbrook, 2001; C.M. pers. obs.). This trait may thus be phylogenetically inherited between horses and rhinos only, or results of a convergence towards a knee-locking apparatus (which has yet to be demonstrated for rhinos).

On the tibia, the massive development of the tibial tuberosity seem more pronounced among African species than in Asiatic ones. The angle between the tibial plateau and the shaft axis is interpreted as a functional character linked to the limb posture (Lessertisseur & Saban, 1967): a plateau caudally lowered may reflect an angulated limb associated to a cursorial habit, whereas an horizontal plateau tends to indicate more columnar limbs. Here, despite a slight change in the plateau orientation between light and heavy rhino species, this trait seems more likely related to phylogeny, African species having a more horizontal plateau than African ones. Similarly, on the distal epiphysis, the rectangular shape of the articular surface for the talus is encountered mainly in the three Asiatic species and not in African specimens.

Role of the ecology

Phylogenetically related rhinos share biotopes with important similarities, making it difficult to accurately assess the environmental effect on bone shape. Furthermore, as historical ranges and habitats of rhinos have been drastically reduced and modified under human pressure (Hillman-Smith & Groves, 1994; Dinerstein, 2011; Groves & Leslie, 2011; Rookmaaker & Antoine, 2013), ecological inferences must be assessed with caution regarding the current rhino biotopes. The related *C. simum* and *D. bicornis* both live in African savannas and display a common general bone morphotype (see above). *D. bicornis* is a ubiquitous species, often visiting both open savannas and clear forests and browsing various vegetal species, whereas *C. simum* is an open grassland grazer (Dinerstein, 2011). The same assessment can be done for the two *Rhinoceros* species, closely phylogenetically related and sharing an important part of their historical geographic range. Despite their strong affinity with water, their ecological preferences are quite different, *R. unicornis* feeding frequently in semi-open floodplains whereas *R. sondaicus* prefers denser forests. *R. sondaicus* and *D. sumatrensis* share a similar lifestyle in dense and closed forest biotopes but only their humerus, femur and fibula tend to display slight shape similarities. If long bone shape is impacted by environmental factors, these constraints are difficult to distinguish from the ones linked to phylogeny. This tends to confirm previous observations indicating that rhino long bones can hardly be used as accurate environmental markers (Guérin, 1980; Eisenmann & Guérin, 1984).

Shape variation, evolutionary allometry and functional implications

Increase in body size and mass between the lightest and heaviest rhinos is associated with a global broadening of the limb long bones, with a clear enlargement of both the diaphysis and epiphyses, confirming previous general observations on different mammalian clades (Bertram & Biewener, 1990, 1992). However, this broadening is not uniform for all the bones. It is directed both medio-laterally and cranio-caudally for the humerus (especially for the proximal part), and mainly medio-laterally for the radius and the femur. Conversely, for the ulna, tibia and fibula, we rather observe a cranio-caudal enlargement, particularly visible on the proximal part of the tibia.

Forelimb bones

The difference between high and low size among extant rhinos is expressed on the humerus by a general enlargement in both cranio-caudal and medio-lateral directions, particularly for the proximal first half. This may be related to the constraints exerted both by weight bearing and braking role of the forelimb during locomotion (Dutto et al., 2006). The important development of the lesser tubercle at the expense of the greater tubercle allows both a greater stability of the shoulder articulation, preventing hyperextension, and a larger insertion area for the medial head of the *m. supraspinatus*, also considered as a shoulder stabilizer (Fisher, Scott & Naples, 2007; Watson & Wilson, 2007). This muscle being one of the main extensors of the forelimb (Barone, 2010b), the developed lesser tubercle acts as a strong medial lever arm for extension movements. This configuration has been previously interpreted as a reinforcement to resist the adduction of the arm (Hermanson & MacFadden, 1992). However, the lesser tubercle also displays an important development in *D. bicornis*, more pronounced than in *R. unicornis* and *R. sondaicus*, though these species are heavier and taller. This indicates a possible impact of phylogenetic proximity or similar habitats between the African species (see above). The medio-lateral enlargement of the distal epiphysis observed towards high body size ensures both a greater stability of the elbow articulation and larger insertion areas for the different flexor muscles for the digits (Barone, 2010a). The distal trochlea of the humerus is also subjected to a proximo-distal compression and a medio-lateral extension, increasing the articular surface area to sustain high body mass (Jenkins, 1973).

Zeugopodial paired bones seem to express complementary shape variations linked to body size. Whereas the radius broadens mainly medio-laterally for high body size, the ulna expends in the cranio-caudal direction: they respond conjointly to the increase in body mass and size to form a structure reinforced in all directions, as it has been observed on the humerus. All rhinos have an ulnar proximal epiphysis situated caudally to the radius, while its shaft expends laterally, possibly allowing a medio-lateral weight display. Moreover, almost all the weight is borne by the proximal articular surface of the radius (Bertram & Biewener, 1992), which expends medially and becomes asymmetrical for heavier rhinos. The concave radial tuberosity shows a deep *m. biceps brachii* insertion delivering a strong forearm flexion (Antoine, 2002) and the developed insertion lateral relief offers a greater surface for extensor muscles of the digits. On the ulna, the developed olecranon process constitutes a strong lever arm for forearm extensors such as the *m. triceps brachii* and the *m. anconeus*. The anconeus process, although cranially reduced, prevents a complete extension of the forearm (Hildebrand, 1974). The distal epiphysis shows a reduction of both radial and ulnar styloid processes towards high body proportions, adding a medio-lateral degree of freedom to the wrist articulation. However, the proximally reduced articular surface for the scaphoid limits the cranio-caudal wrist flexion. These morphological traits allow the foot to bear the weight on different substrates while limiting the risk of wrist hyperflexion (Domming, 2002).

Hind limb bones

In the hind limb, the femur expends mainly in the medio-lateral direction for high body mass and size, tending to indicate a stronger resistance both linked to body propulsion and weight bearing (Lessertisseur & Saban, 1967), exerted in the medio-lateral direction (Hildebrand, 1974). The medio-lateral reinforcement of the femur is mainly located under the head and the neck, responding to a concomitant enlargement of the medial condyle on the distal epiphysis, both indicating an increase of the body load near the sagittal plane. The more distal location of the lesser trochanter improves the lever arm of the *mm. psoas major* and *iliacus*, developing slower but stronger hip flexions (Hildebrand, 1974; Polly, 2007). The same phenomenon is observed with the third trochanter, situated at half of the shaft – contrary to in cursorial Perissodactyla like equids, where the third trochanter is more proximally situated (Hermanson & Macfadden, 1996; Holbrook, 2001; Barone, 2010a). The extreme development of the third trochanter associated

with a disto-lateral development of the greater trochanter also create a large lever arm for the *fascia glutea*, the *mm. gluteus superficialis* and *gluteus medius* allowing strong hip flexion and abduction. This association seems maximal for *R. unicornis*, where the greater and third trochanters can be fused by a bony bridge. At the opposite, the greater trochanter is less proximally developed than in related groups like horses and tapirs (Hermanson & Macfadden, 1996; MacLaren & Nauwelaerts, 2016): as this trochanter is the insertion area for the *m. gluteus medius*, the main extensor of the hip, the extension in rhinos seems less powerful than in cursorial perissodactyls. On the distal epiphysis, the lateral torsion of the rotation axis of the trochlea in heavy rhinos also indicates a more laterally deviated position of the knee: this conformation may improve weight bearing, deporting the body mass laterally to the body, as previously observed on a study of pressure patterns of the feet in *C. simum* (Panagiotopoulou, Pataky & Hutchinson, 2018). No real difference on the bone curvature related to body proportion was noticed, confirming previous observations on the independence of femur curvature with regard to body mass increase in quadrupedal mammals (Bertram & Biewener, 1992).

On the zeugopodial elements, when the proximal epiphysis of the tibia broadens cranio-caudally, the one of the fibula one is reduced in this direction, despite an increased general robustness. The proximal epiphysis of the fibula is also oriented far more cranially than in lighter specimens. The enlargement of the tibial plateau thus seems to involve a relative reduction in size of the fibula head. The distal epiphyses of both bones variate conjointly too, with a broadening mainly expressed in the cranio-caudal direction. The medial condyle of the tibial plateau enlarges strongly, resulting into an asymmetrical proximal epiphysis. Moreover, the broadening of the tibial tuberosity correlates with a stronger and larger patellar ligament, reinforcing the knee articulation and the lever arm created by the patella (Hildebrand, 1974). On the distal epiphysis, the two malleoli are more medio-laterally inflated but less distally expended, allowing the tarsal articulation to move more freely in heavier rhinos (Lessertisseur & Saban, 1967). This trait is associated to a slightly shallower distal articular surface, conferring more important degrees of freedom to the ankle articulation for high body size and mass (Polly, 2007). This observation is coherent with similar analyses conducted on rhino ankle bones (Etienne et al., submitted).

In addition to the reduction of the proximal epiphysis, the fibula displays a straighter diaphysis for large rhinos as opposed to the greatly curved one for lighter rhinos. This is consistent with

previous observations: although the fibula was not considered in their study, Bertram & Biewener (1992) noted a decrease of the tibia curvature while body mass increases among terrestrial mammals. In our rhino sample, the tibia shows a very slight straightening of the diaphysis. However, this straightening, maybe linked to the load carrying capacity, appears to be more pronounced on the fibula.

Differences between body mass and body size

As the exact body mass was only known for five specimens of our sample, we were not able to precisely express the shape variation regarding the animal's individual weight. However, theoretical bone shape obtained with mean body mass are very similar to the ones obtained with centroid size (see above). Comparing the values of the centroid size and mean body mass highlights some interspecific differences: if *D. sumatrensis*, the smallest rhino, has the lowest values for both centroid size and body mass, the tallest *R. unicornis* displays the highest values of centroid size in most of the cases, confirming its higher general size among modern rhinos (Guérin, 1980; Dinerstein, 2011), despite a mean body mass (2,000 kg) lower than that of *C. simum* (2,300 kg). Furthermore, the centroid size of an isolated bone may neither reflect the actual global size of an animal, nor be strictly correlated with its body mass. This is particularly visible for taxa displaying brachypodial adaptation (i.e. shortening of limb length relatively to the body size), as it is the case for modern hippos or some fossil rhinos like *Brachypotherium* or *Teleoceras* (Cerdeño, 1998). However, as bone size and body mass are intimately entangled (Berner, 2011), the centroid size of isolated bones may still constitute a useful body mass approximation when precise body mass remains unknown and if considered cautiously. This is coherent with previous results obtained on cranial shape data indicating a marked correlation between body mass and centroid size (both of the skull and mandible) for many mammalian lineages, especially modern rhinos (Cassini, Vizcaíno & Bargo, 2012).

Limb bone shape and graviportality

One of the criteria defining graviportality are the straight and columnar limbs (Gregory, 1912; Osborn, 1929; Biewener, 1989b). Rhino's limb long bones do not display a true columnar organisation (Osborn, 1900, 1929). Morphological changes between light and heavy rhino species do not imply a clear change in the orientation of the articular facets: the elbow joint

remains unable to completely open like the elephant's one and the knee remains markedly angulated. Only the humeral proximal epiphysis displays a tenuous orientation change between light and heavy rhinos, allowing a more slightly vertical orientation of this bone for *C. simum* and *R. unicornis*.

Limb straightness can results from the reorientation of the trochlear notch of the ulna in the dorsal direction, allowing an efficient support of the humerus (Gregory, 1912), as in proboscideans (Christiansen, 1999). Our sample tends to indicate instead that the radius is the main support of the body weight in the forelimb among modern rhinos. The shape of the radius becomes gradually more robust from light to heavy rhinos, with a strong medial reinforcement of the proximal epiphysis. The particular role of the radius was previously highlighted among a large sample of mammal clades (Bertram & Biewener, 1992), its vertical position being opposed to ground reaction forces. This supportive role of the radius is widespread among Ungulata and remains of importance even in larger fossil rhinos like Elasmotheriinae (Antoine, 2002) and Paraceratheriidae (Qiu & Wang, 2007; Prothero, 2013). Unlike in elephants, increase in body mass among rhinos is correlated to a more important supportive role of the radius. At the opposite, the ulna role has not been extendedly explored in morphofunctional studies. Our work underlines the complementary role of the ulna relatively to the radius, providing more lateral and caudal weight bearing by an enlargement in the dorso-palmar direction. In this regard, the forearm conformation in rhinos is close to the one encountered in hippos (Fisher, Scott & Naples, 2007).

Forelimb elements bear more weight than hind limb ones (Lessertisseur & Saban, 1967; Hildebrand, 1974; Polly, 2007) and play an additional braking role during locomotion, particularly proximal elements (Dutto et al., 2006). Forelimb bones such as the humerus thus need to be reinforced in all directions in order to support these higher weight constraints in heavier animals. Hind limb bone shape is affected differently than in forelimb by increases in body mass and size. Hind limb bears relatively less weight than the forelimb and plays an additional propulsive role during locomotion (Lessertisseur & Saban, 1967; Hildebrand, 1974; Barone, 2010a). The femur displays important reinforcement and development of strong lever arms in large rhino species, possibly to support increasing stress due to locomotion and body mass, but the variations in shape of the tibia and the fibula seem driven as much by the body size

as by the phylogenetic influence. The shape of the fibula is particularly variable within several rhino species, questioning its functional role but also the factors driving this strong intraspecific variation. It has been shown that the human fibula plays, in addition to its ankle stabilizer role, a small but important weight bearing role, receiving one sixth of the load applied to the knee (Lambert, 1971; Takebe et al., 1984). In horses, the diaphysis of the fibula is absent and the malleolus is fused with the tibia, ensuring mainly ankle stabilization (Barone, 2010a). Rhino's fibula, contrary to the horse's one, ensures both load bearing and talus stabilization roles (Polly, 2007). In addition, this bone often bears crests along the diaphysis with no apparent correlation with weight bearing (see above). These crest developments may be due to individual variations in bone development, without clear functional implications, but this first analysis does not allow us to state on this question.

Bertram & Biewener (1990, 1992) and Polly (2007) previously called "allometry increase" the tendency to body size and mass rise among terrestrial mammals. Although reduced, this allometry clearly affects our sample (Tables 6 and 7). In addition, the robustness increase is associated with a slight relative length reduction of the bone for larger rhinos (Guérin, 1980), a general trend observed among heavy mammals (Christiansen, 1999). Another trait associated to body size augmentation among extant rhino species is the expansion of the epiphysis medial parts (e.g., medial epicondyle and trochlear lip on the humerus, medial glenoid cavity on the radius, medial condyle and trochlear lip on the femur, medial condyle on the tibia). These medial reinforcements result in more asymmetrical bones, potentially increasing parasagittal weight bearing (Barone, 2010a). This conformation is coherent with foot posture during walk: rhino forefeet are placed under the body, close to the sagittal plane of the animal (Paul & Christiansen, 2000). Hind feet are more spaced and oriented laterally, especially for heavy rhinos (Panagiotopoulou et al., 2018), which seems coherent with our observations regarding the rotation axis of the femoral trochlea, oriented more laterally as well. However, the distal articular surface of the tibia displays a broader lateral groove and appears as a counterexample (Figure 5). This lateral broadening of the ankle joint, also observed on the talus (Etienne et al., submitted), may be correlated with the hind limb posture of rhinos: as the pelvic bone is large and the feet are placed under the body and oriented more laterally than forefeet, the legs are not parallel to the sagittal plane (Paul & Christiansen, 2000; C.M. pers. obs.). The vertical forces exerted by the body mass may therefore cross the axis of the tibia. This appears in accordance with the fact that

the forces may be medially higher on the proximal plateau but laterally higher at the ankle joint: this point would need to be tested more precisely *in vivo*. As studies of pressure patterns indicate that foot pressure is more intense laterally (Pfistermüller, Walzer & Licka, 2011; Panagiotopoulou, Pataky & Hutchinson, 2018), it will be crucial to explore relations that exist between stylopodium, zeugopodium and autopodium organisation in the complete limb, as well as the gait and posture of the rhinos.

Conclusion

This study conducted on the limb long bones among modern rhinos highlights the occurrence of three distinct morphotypes. These latter reflect phylogenetic relationships, and also differently impacted by body size and mass. The shape of the stylopodium bones, though affected by body mass variations, remains highly constrained by phylogeny, whereas it is more strongly impacted by body mass and size in zeugopodial bones, especially the radius and ulna, which underlies their important role in weight bearing. As for the shape of the tibia, it is influenced by both changes in body mass and size, and phylogeny. The unique pattern of the fibula reveals that, beyond the important intraspecific variation, this bone also plays a substantial role in weight bearing. Quick comparisons with hippos and elephants show clear differences and convergences and highlight the interest of investigating shape variation in other heavy mammal taxa. This would enable to describe the different ways to sustain an increase of body mass in mammals and, eventually, to sharpen the concept of “graviportality”.

Acknowledgments

The authors would like to warmly thank all the curators of the visited institutions for granting access to the studied specimens: Catriona West, Rachel Jennings, Mike Cobb (Powell Cotton Museum, Birchington-on-Sea, UK), Didier Berthet (Centre de Conservation et d’Étude des Collections, Musée des Confluences, Lyon, France), Yves Laurent (Muséum d’Histoire Naturelle de Toulouse, Toulouse, France), Joséphine Lesur, Aurélie Verguin, Salvador Bailon (Muséum National d’Histoire Naturelle, Paris, France), Roberto Portela-Miguez (Natural History Museum, London, UK), Frank Zachos, Alexander Bibl (Naturhistorisches Museum Wien, Vienna, Austria), Olivier Pauwels, Sébastien Bruaux (Royal Belgian Institute of Natural Sciences,

Brussels, Belgium), Emmanuel Gilissen (Royal Museum for Central Africa, Tervuren, Belgium), Anneke H. van Heteren (Zoologische Staatssammlung München, Munich, Germany) and John Hutchinson for providing us CT-scan data coming from the National Museums Scotland (Edinburgh, UK), the University of California Museum of Paleontology (Berkeley, USA) and the University Museum of Zoology Cambridge (Cambridge, UK). C.M. acknowledges Arnaud Delapré (MNHN, Paris, France) for significant help in 3D data reconstruction and management, Cyril Étienne, Rémi Lefebvre, Romain Pintore (MNHN, Paris, France) for constructive discussions and advices on R programming, data analyses and interpretations. This work was funded by the European Research Council and is part of the GRAVIBONE project (ERC-2016-STG-715300).

Author contributions

All authors designed the frame of the study. C.M. did most of the data acquisition with additions from A.H. C.M. performed the analyses under the guidance of R.C. C.M. drafted the manuscript. All authors reviewed and contributed to the final manuscript, read it and approved it.

References

Adams DC. 2014. A generalized K statistic for estimating phylogenetic signal from shape and other high-dimensional multivariate data. *Systematic Biology* 63:685–697. DOI: 10.1093/sysbio/syu030.

Adams DC, Collyer M, Kaliontzopoulou A. 2018. *Geometric Morphometric Analyses of 2D/3D Landmark Data*.

Adams DC, Otárola-Castillo E. 2013. geomorph: an r package for the collection and analysis of geometric morphometric shape data. *Methods in Ecology and Evolution* 4:393–399. DOI: 10.1111/2041-210X.12035.

957 Adams DC, Rohlf FJ, Slice DE. 2004. Geometric morphometrics: Ten years of progress
958 following the 'revolution.' *Italian Journal of Zoology* 71:5–16. DOI:
959 10.1080/11250000409356545.
960 Agisoft. 2018. *PhotoScan Professional Edition*. Agisoft.
961 Alexander RMcN, Pond CM. 1992. Locomotion and bone strength of the white rhinoceros,
962 *Ceratotherium simum*. *Journal of Zoology* 227:63–69. DOI: 10.1111/j.1469-
963 7998.1992.tb04344.x.
964 Antoine P-O. 2002. *Phylogénie et évolution des Elasmotheriina (Mammalia, Rhinocerotidae)*.
965 Publications scientifiques du Muséum.
966 Antoine P-O, Duranthon F, Welcomme J-L. 2003. *Alicornops* (Mammalia, Rhinocerotidae) dans
967 le Miocène supérieur des Collines Bugti (Balouchistan, Pakistan): implications
968 phylogénétiques. *Geodiversitas* 25:575–603.
969 Artec 3D. 2018. *Artec Studio Professional*. Artec 3D.
970 Averianov A, Danilov I, Jin J, Wang Y. 2017. A new amynodontid from the Eocene of South
971 China and phylogeny of Amynodontidae (Perissodactyla: Rhinocerotoidea). *Journal of*
972 *Systematic Palaeontology* 15:927–945. DOI: 10.1080/14772019.2016.1256914.
973 Baker J, Meade A, Pagel M, Venditti C. 2015. Adaptive evolution toward larger size in
974 mammals. *Proceedings of the National Academy of Sciences* 112:5093–5098. DOI:
975 10.1073/pnas.1419823112.
976 Barone R. 2010a. *Anatomie comparée des mammifères domestiques. Tome 1 : Ostéologie*. Paris:
977 Vigot Frères.
978 Barone R. 2010b. *Anatomie comparée des mammifères domestiques. Tome 2 : Arthrologie et*
979 *myologie*. Paris: Vigot Frères.

980 Becker D. 2003. Paléoécologie et paléoclimats de la molasse du Jura (oligo-miocène). Université
981 de Fribourg.
982 Becker D, Antoine P-O, Maridet O. 2013. A new genus of Rhinocerotidae (Mammalia,
983 Perissodactyla) from the Oligocene of Europe. *Journal of Systematic Palaeontology*
984 11:947–972. DOI: 10.1080/14772019.2012.699007.
985 Becker D, Bürgin T, Oberli U, Scherler L. 2009. *Diaceratherium lemanense* (Rhinocerotidae)
986 from Eschenbach (eastern Switzerland): systematics, palaeoecology,
987 palaeobiogeography. *Neues Jahrbuch für Geologie und Paläontologie-Abhandlungen*
988 254:5–39. DOI: 10.1127/0077-7749/2009/0002.
989 Beddard FE, Treves F. 1889. On the Anatomy of *Rhinoceros sumatrensis*. *Proceedings of the*
990 *Zoological Society of London* 57:7–25. DOI: 10.1111/j.1469-7998.1889.tb06740.x.
991 Berger J. 1994. Science, Conservation, and Black Rhinos. *Journal of Mammalogy* 75:298–308.
992 DOI: 10.2307/1382548.
993 Berner D. 2011. Size correction in biology: how reliable are approaches based on (common)
994 principal component analysis? *Oecologia* 166:961–971. DOI: 10.1007/s00442-011-1934-
995 z.
996 Bertram JEA, Biewener AA. 1990. Differential scaling of the long bones in the terrestrial
997 carnivora and other mammals. *Journal of Morphology* 204:157–169. DOI:
998 10.1002/jmor.1052040205.
999 Bertram JEA, Biewener AA. 1992. Allometry and curvature in the long bones of quadrupedal
1000 mammals. *Journal of Zoology* 226:455–467. DOI: 10.1111/j.1469-7998.1992.tb07492.x.
1001 Biewener AA. 1989a. Mammalian Terrestrial Locomotion and Size. *BioScience* 39:776–783.
1002 DOI: 10.2307/1311183.

1003 Biewener AA. 1989b. Scaling body support in mammals: limb posture and muscle mechanics.
1004 *Science* 245:45–48. DOI: 10.1126/science.2740914.
1005 de Blainville H-MD, Nicard P. 1839. *Ostéographie, ou Description iconographique comparée*
1006 *du squelette et du système dentaire des mammifères récents et fossiles pour servir de base*
1007 *à la zoologie et à la géologie. Tome 3*. Paris: J.B. Baillère & Fils.
1008 Bokma F, Godinot M, Maridet O, Ladevèze S, Costeur L, Solé F, Gheerbrant E, Peigné S,
1009 Jacques F, Laurin M. 2016. Testing for Depéret's Rule (Body Size Increase) in Mammals
1010 using Combined Extinct and Extant Data. *Systematic Biology* 65:98–108. DOI:
1011 10.1093/sysbio/syv075.
1012 Botton-Divet L, Cornette R, Fabre A-C, Herrel A, Houssaye A. 2016. Morphological Analysis of
1013 Long Bones in Semi-aquatic Mustelids and their Terrestrial Relatives. *Integrative and*
1014 *Comparative Biology* 56:1298–1309. DOI: 10.1093/icb/icw124.
1015 Cappellini E, Welker F, Pandolfi L, Madrigal JR, Fotakis A, Lyon D, Mayar VLM,
1016 Bukhsianidze M, Jersie-Christensen RR, Mackie M, Ginolhac A, Ferring R, Tappen M,
1017 Palkopoulou E, Samodova D, Ruther PL, Dickinson MR, Stafford T, Chan YL,
1018 Gotherstrom A, Nathan SK, Heintzman PD, Kapp JD, Kirillova I, Moodley Y, Agusti J,
1019 Kahlke R-D, Kiladze G, Martinez-Navarro B, Liu S, Velasco MS, Sinding M-HS,
1020 Kelstrup CD, Allentoft ME, Krogh A, Orlando L, Penkman K, Shapiro B, Rook L, Dalen
1021 L, Gilbert MTP, Olsen JV, Lordkipanidze D, Willerslev E. 2018. Early Pleistocene
1022 enamel proteome sequences from Dmanisi resolve *Stephanorhinus* phylogeny.
1023 *bioRxiv*:407692. DOI: 10.1101/407692.

1024 Carrano MT. 1999. What, if anything, is a cursor? Categories versus continua for determining
1025 locomotor habit in mammals and dinosaurs. *Journal of Zoology* 247:29–42. DOI:
1026 10.1111/j.1469-7998.1999.tb00190.x.
1027 Cassini GH, Vizcaíno SF, Bargo MS. 2012. Body mass estimation in Early Miocene native
1028 South American ungulates: a predictive equation based on 3D landmarks. *Journal of*
1029 *Zoology* 287:53–64. DOI: 10.1111/j.1469-7998.2011.00886.x.
1030 Cerdeño E. 1995. Cladistic analysis of the family Rhinocerotidae (Perissodactyla). American
1031 Museum novitates ; no. 3143.
1032 Cerdeño E. 1998. Diversity and evolutionary trends of the Family Rhinocerotidae
1033 (Perissodactyla). *Palaeogeography, Palaeoclimatology, Palaeoecology* 141:13–34. DOI:
1034 10.1016/S0031-0182(98)00003-0.
1035 Christiansen P. 1999. Scaling of mammalian long bones: small and large mammals compared.
1036 *Journal of Zoology* 247:333–348. DOI: 10.1111/j.1469-7998.1999.tb00996.x.
1037 Cignoni P, Callieri M, Corsini M, Dellepiane M, Ganovelli F, Ranzuglia G. 2008. *MeshLab: an*
1038 *Open-Source Mesh Processing Tool*. The Eurographics Association. DOI:
1039 http://dx.doi.org/10.2312/LocalChapterEvents/ItalChap/ItalianChapConf2008/129-136.
1040 Colyn M. 1980. Ostéologie descriptive de *Ceratotherium simum cottoni* Lydekker, 1908. Faculté
1041 des Sciences, Bruxelles, 201 p.
1042 Coombs Walter P. 1978. Theoretical Aspects of Cursorial Adaptations in Dinosaurs. *The*
1043 *Quarterly Review of Biology* 53:393–418. DOI: 10.1086/410790.
1044 Cuvier G. 1812. *Recherches sur les ossements fossiles de quadrupèdes. Tome 2*. Paris:
1045 Deterville.
1046 Depéret C. 1907. *Les transformations du monde animal*. Paris: Flammarion.

1047 Dinerstein E. 1991. Sexual Dimorphism in the Greater One-Horned Rhinoceros (*Rhinoceros*
1048 *unicornis*). *Journal of Mammalogy* 72:450–457. DOI: 10.2307/1382127.
1049 Dinerstein E. 2011. Family Rhinocerotidae (Rhinoceroses). In: *Handbook of the Mammals of the*
1050 *World*. Barcelona: Don E. Wilson & Russel A. Mittermeier, 144–181.
1051 Domming DP. 2002. The terrestrial posture of desmostylians. *Smithsonian Contributions to*
1052 *Paleobiology* 93.
1053 Dutto DJ, Hoyt DF, Clayton HM, Cogger EA, Wickler SJ. 2006. Joint work and power for both
1054 the forelimb and hindlimb during trotting in the horse. *Journal of Experimental Biology*
1055 209:3990–3999. DOI: 10.1242/jeb.02471.
1056 Eisenmann V, Guérin C. 1984. Morphologie fonctionnelle et environnement chez les
1057 périssodactyles. *Geobios* 17:69–74. DOI: 10.1016/S0016-6995(84)80158-8.
1058 Etienne C, Mallet C, Cornette R, Houssaye A. submitted. Patterns and drivers of tarsus shape
1059 variation among extant and extinct Rhinocerotidae and their relatives: a morphometrical
1060 investigation.
1061 Fau M, Cornette R, Houssaye A. 2016. Photogrammetry for 3D digitizing bones of mounted
1062 skeletons: Potential and limits. *Comptes Rendus Palevol* 15:968–977. DOI:
1063 10.1016/j.crpv.2016.08.003.
1064 Fernando P, Polet G, Foead N, Ng LS, Pastorini J, Melnick DJ. 2006. Genetic diversity,
1065 phylogeny and conservation of the Javan rhinoceros (*Rhinoceros sondaicus*).
1066 *Conservation Genetics* 7:439–448. DOI: 10.1007/s10592-006-9139-4.
1067 Fisher RE, Scott KM, Adrian B. 2010. Hind limb myology of the common hippopotamus,
1068 *Hippopotamus amphibius* (Artiodactyla: Hippopotamidae). *Zoological Journal of the*
1069 *Linnean Society* 158:661–682. DOI: 10.1111/j.1096-3642.2009.00558.x.

1070 Fisher RE, Scott KM, Naples VL. 2007. Forelimb myology of the pygmy hippopotamus
1071 (*Choeropsis liberiensis*). *The Anatomical Record* 290:673–693. DOI: 10.1002/ar.20531.
1072 Gaudry M. 2017. Molecular phylogenetics of the rhinoceros clade and evolution of UCP1
1073 transcriptional regulatory elements across the mammalian phylogeny. Master of Science
1074 Thesis. Winnipeg: University of Manitoba.
1075 Goodall C. 1991. Procrustes Methods in the Statistical Analysis of Shape. *Journal of the Royal*
1076 *Statistical Society: Series B (Methodological)* 53:285–321. DOI: 10.1111/j.2517-
1077 6161.1991.tb01825.x.
1078 Gower JC. 1975. Generalized procrustes analysis. *Psychometrika* 40:33–51. DOI:
1079 10.1007/BF02291478.
1080 Gregory WK. 1912. Notes on the Principles of Quadrupedal Locomotion and on the Mechanism
1081 of the Limbs in Hoofed Animals. *Annals of the New York Academy of Sciences* 22:267–
1082 294. DOI: 10.1111/j.1749-6632.1912.tb55164.x.
1083 Groves CP. 1967a. Geographic variation in the black rhinoceros, *Diceros bicornis* (L, 1758).
1084 *Zeitschrift fur Saugetierkunde* 32:267–276.
1085 Groves CP. 1967b. On the rhinoceroses of South-East Asia. *Saugetierkundliche Mitteilungen*
1086 15:221–237.
1087 Groves CP. 1972. *Ceratotherium simum*. *Mammalian Species*:1–6. DOI: 10.2307/3503966.
1088 Groves CP. 1982. The skulls of Asian rhinoceroses: Wild and captive. *Zoo Biology* 1:251–261.
1089 DOI: 10.1002/zoo.1430010309.
1090 Groves CP, Kurt F. 1972. *Dicerorhinus sumatrensis*. *Mammalian Species*:1–6. DOI:
1091 10.2307/3503818.

1092 Groves CP, Leslie DM. 2011. *Rhinoceros sondaicus* (Perissodactyla: Rhinocerotidae).
1093 *Mammalian Species* 43:190–208. DOI: 10.2307/mammalianspecies.43.1.190.
1094 Guérin C. 1980. Les Rhinocéros (Mammalia, Perissodactyla) du Miocène terminal au
1095 Pléistocène supérieur en Europe occidentale. Comparaison avec les espèces actuelles.
1096 Documents du Laboratoire de Géologie de l'Université de Lyon Thesis.
1097 Guérin C. 1982. Les Rhinocerotidae (Mammalia, Perissodactyla) du Miocène terminal au
1098 Pleistocène supérieur d'Europe Occidentale comparés aux espèces actuelles: Tendances
1099 évolutives et relations phylogénétiques. *Geobios* 15:599–605. DOI: 10.1016/S0016-
1100 6995(82)80077-6.
1101 Gunz P, Mitteroecker P. 2013. Semilandmarks: a method for quantifying curves and surfaces.
1102 *Hystrix, the Italian Journal of Mammalogy* 24:103–109.
1103 Gunz P, Mitteroecker P, Bookstein FL. 2005. Semilandmarks in Three Dimensions. In: *Modern*
1104 *Morphometrics in Physical Anthropology*. Developments in Primatology: Progress and
1105 Prospects. Springer, Boston, MA, 73–98. DOI: 10.1007/0-387-27614-9_3.
1106 Heissig K. 1972. Paläontologische und geologische Untersuchungen im Tertiär von Pakistan – 5.
1107 Rhinocerotidae (Mammalia) aus den unteren und mittleren Siwalik-Schichten.
1108 *Abhandlungen der Bayerischen Akademie der Wissenschaften, Mathematisch-*
1109 *naturwissenschaftliche Klasse, München* 152:1–112.
1110 Heissig K. 2012. Les Rhinocerotidae (Perissodactyla) de Sansan. In: *Mammiferes de Sansan*.
1111 Mémoires du Muséum national d'histoire naturelle. Paris, 317–485.
1112 Hermanson JW, MacFadden BJ. 1992. Evolutionary and functional morphology of the shoulder
1113 region and stay-apparatus in fossil and extant horses (Equidae). *Journal of Vertebrate*
1114 *Paleontology* 12:377–386. DOI: 10.1080/02724634.1992.10011466.

1115 Hermanson JW, Macfadden BJ. 1996. Evolutionary and functional morphology of the knee in
1116 fossil and extant horses (Equidae). *Journal of Vertebrate Paleontology* 16:349–357. DOI:
1117 10.1080/02724634.1996.10011321.
1118 Hildebrand M. 1974. *Analysis of vertebrate structure*. New York: John Wiley & Sons.
1119 Hillman-Smith AKK, Groves CP. 1994. *Diceros bicornis*. *Mammalian Species*:1–8. DOI:
1120 10.2307/3504292.
1121 Holbrook LT. 2001. Comparative osteology of early Tertiary tapiromorphs (Mammalia,
1122 Perissodactyla). *Zoological Journal of the Linnean Society* 132:1–54. DOI:
1123 10.1111/j.1096-3642.2001.tb02270.x.
1124 Janis CM, Shoshitaishvili B, Kambic R, Figueirido B. 2012. On their knees: distal femur
1125 asymmetry in ungulates and its relationship to body size and locomotion. *Journal of*
1126 *Vertebrate Paleontology* 32:433–445. DOI: 10.1080/02724634.2012.635737.
1127 Jenkins FA. 1973. The functional anatomy and evolution of the mammalian humero-ulnar
1128 articulation. *American Journal of Anatomy* 137:281–297. DOI: 10.1002/aja.1001370304.
1129 Klingenberg CP. 2016. Size, shape, and form: concepts of allometry in geometric
1130 morphometrics. *Development Genes and Evolution* 226:113–137. DOI: 10.1007/s00427-
1131 016-0539-2.
1132 Lambert KL. 1971. The weight-bearing function of the fibula. A strain gauge study. *The Journal*
1133 *of Bone and Joint Surgery. American Volume* 53:507–513.
1134 Langman VA, Roberts TJ, Black J, Maloiy GM, Heglund NC, Weber JM, Kram R, Taylor CR.
1135 1995. Moving cheaply: energetics of walking in the African elephant. *Journal of*
1136 *Experimental Biology* 198:629–632.

1137 Laurie WA, Lang EM, Groves CP. 1983. *Rhinoceros unicornis*. *Mammalian Species*:1–6. DOI:
1138 10.2307/3504002.
1139 Lessertisseur J, Saban R. 1967. Le squelette. Squelette appendiculaire. In: *Traité de Zoologie.*
1140 *Tome XVI, Fasicule 1: Mammifères.* Paris: Grassé Pierre-Paul, 298–1123.
1141 MacFadden BJ. 2005. Diet and habitat of toxodont megaherbivores (Mammalia, Notoungulata)
1142 from the late Quaternary of South and Central America. *Quaternary Research* 64:113–
1143 124. DOI: 10.1016/j.yqres.2005.05.003.
1144 MacLaren JA, Nauwelaerts S. 2016. A three-dimensional morphometric analysis of upper
1145 forelimb morphology in the enigmatic tapir (Perissodactyla: Tapirus) hints at subtle
1146 variations in locomotor ecology. *Journal of Morphology* 277:1469–1485. DOI:
1147 10.1002/jmor.20588.
1148 Mallison H, Wings O. 2014. Photogrammetry in Paleontology - A practical guide. *Journal of*
1149 *Paleontological Techniques*.
1150 Maynard Smith J, Savage RJG. 1956. Some locomotory adaptations in Mammals. *Zoological*
1151 *Journal of the Linnean Society* 42:603–622. DOI: 10.1111/j.1096-3642.1956.tb02220.x.
1152 McMahon T. 1973. Size and Shape in Biology: Elastic criteria impose limits on biological
1153 proportions, and consequently on metabolic rates. *Science* 179:1201–1204. DOI:
1154 10.1126/science.179.4079.1201.
1155 Osborn HF. 1900. The Angulation of the Limbs of Proboscidia, Dinocerata, and Other
1156 Quadrupeds, in Adaptation to Weight. *The American Naturalist* 34:89–94. DOI:
1157 10.1086/277565.
1158 Osborn HF. 1929. *The Titanotheres of ancient Wyoming, Dakota, and Nebraska*. Government
1159 Printing Office.

1160 Panagiotopoulou O, Pataky TC, Hutchinson JR. 2018. Foot pressure distribution in white
1161 rhinoceroses (*Ceratotherium simum*) during walking. *PeerJ Inc.* DOI:
1162 10.7287/peerj.preprints.27365v1.
1163 Paradis E, Blomberg SP, Bolker B, Brown J, Claude J, Cuong HS, Desper R, Didier G, Durand
1164 B, Dutheil J, Ewing J, Gascuel O, Guillerme T, Heibl C, Ives A, Jones B, Krah F,
1165 Lawson D, Lefort V, Legendre P, Lemon J, Marcon E, McCloskey R, Nylander J,
1166 Opgen-Rhein R, Popescu A-A, Royer-Carenzi M, Schliep K, Strimmer K, de Vienne D.
1167 2018. *Ape: Analyses of Phylogenetics and Evolution*.
1168 Paul GS, Christiansen P. 2000. Forelimb posture in neoceratopsian dinosaurs: implications for
1169 gait and locomotion. *Paleobiology* 26:450–465. DOI: 10.1666/0094-
1170 8373(2000)026<0450:FPINDI>2.0.CO;2.
1171 Petti FM, Avanzini M, Belvedere M, De Gasperi M, Ferretti P, Girardi S, Remondino F,
1172 Tomasoni R. 2008. Digital 3D modelling of dinosaur footprints by photogrammetry and
1173 laser scanning techniques: integrated approach at the Coste dell'Anglone tracksite (Lower
1174 Jurassic, Southern Alps, Northern Italy). *Studi Trentini di Scienze Naturali - Acta*
1175 *Geologia* 83:303–315.
1176 Pfistermüller R, Walzer C, Licka T. 2011. From Chitwan to Vienna – How do gait parameters
1177 change in a pair of Indian Rhinos (*Rhinoceros unicornis*) coming from semi-wild
1178 conditions to a European Zoo? In: *Proceedings of the 2011 International Elephant and*
1179 *Rhino Conservation and Research Symposium*. Rotterdam.
1180 Piras P, Maiorino L, Raia P, Marcolini F, Salvi D, Vignoli L, Kotsakis T. 2010. Functional and
1181 phylogenetic constraints in Rhinocerotinae craniodental morphology. *Evolutionary*
1182 *Ecology Research* 12:897–928.

1183 Polly PD. 2007. Limbs in mammalian evolution. Chapter 15. In: *Fins into Limbs: Evolution,*
1184 *Development, and Transformation*. Chicago: Brian K. Hall, 245–268.
1185 Prothero DR. 1998. Rhinocerotidae. In: *Evolution of Tertiary Mammals of North America:*
1186 *Volume 1, Terrestrial Carnivores, Ungulates, and Ungulate Like Mammals*. Cambridge
1187 University Press, 595–605.
1188 Prothero DR. 2013. *Rhinoceros Giants: The Paleobiology of Indricotheres*. Indiana University
1189 Press.
1190 Prothero DR, Manning EM, Hanson BC. 1986. The phylogeny of the Rhinocerotoidea
1191 (Mammalia, Perissodactyla). *Zoological Journal of the Linnean Society* 87:341–366.
1192 Prothero DR, Schoch RM. 1989. *The evolution of perissodactyls*. New York: Oxford University
1193 Press.
1194 Prothero DR, Sereno PC. 1982. Allometry and Paleoecology of Medial Miocene Dwarf
1195 Rhinoceroses from the Texas Gulf Coastal Plain. *Paleobiology* 8:16–30.
1196 Qiu Z-X, Wang B-Y. 2007. *Paracerathere Fossils of China*. Beijing.
1197 R Core Team. 2014. *R: a language and environment for statistical computing*. Vienna: R
1198 Foundation for Statistical Computing.
1199 Raia P, Carotenuto F, Passaro F, Fulgione D, Fortelius M. 2012. Ecological Specialization in
1200 Fossil Mammals Explains Cope's Rule. *The American Naturalist* 179:328–337. DOI:
1201 10.1086/664081.
1202 Remondino F, Rizzi A, Girardi S, Petti FM, Avanzini M. 2010. 3D Ichnology—recovering
1203 digital 3D models of dinosaur footprints. *The Photogrammetric Record* 25:266–282.
1204 DOI: 10.1111/j.1477-9730.2010.00587.x.

1205 Rohlf FJ, Slice D. 1990. Extensions of the Procrustes Method for the Optimal Superimposition
1206 of Landmarks. *Systematic Biology* 39:40–59. DOI: 10.2307/2992207.
1207 Rookmaaker K, Antoine P-O. 2013. New maps representing the historical and recent distribution
1208 of the African species of rhinoceros: *Diceros bicornis*, *Ceratotherium simum* and
1209 *Ceratotherium cottoni*. *Pachyderm* 0:91–96.
1210 Ross MD. 1984. The influence of gravity on structure and function of animals. *Advances in*
1211 *Space Research* 4:305–314. DOI: 10.1016/0273-1177(84)90575-1.
1212 Sanborn CC, Watkins AR. 1950. Notes on the Malay Tapir and Other Game Animals in Siam.
1213 *Journal of Mammalogy* 31:430–433. DOI: 10.2307/1375112.
1214 Scherler L, Mennecart B, Hiard F, Becker D. 2013. Evolutionary history of hoofed mammals
1215 during the Oligocene–Miocene transition in Western Europe. *Swiss Journal of*
1216 *Geosciences* 106:349–369. DOI: 10.1007/s00015-013-0140-x.
1217 Schlager S. 2018. *Morpho: calculations and vizualisations related to Geometric Morphometrics*.
1218 Scott WB, Jepsen GL. 1941. The Mammalian Fauna of the White River Oligocene. Part V.
1219 Perissodactyla. *Transactions of the American Philosophical Society, New Series* 28:747–
1220 975.
1221 Stein BR, Casinos A. 1997. What is a cursorial mammal? *Journal of Zoology* 242:185–192. DOI:
1222 10.1111/j.1469-7998.1997.tb02939.x.
1223 Stilson KT, Hopkins SSB, Davis EB. 2016. Osteopathology in Rhinocerotidae from 50 Million
1224 Years to the Present. *PLOS ONE* 11:e0146221. DOI: 10.1371/journal.pone.0146221.
1225 Takebe K, Nakagawa A, Minami H, Kanazawa H, Hirohata K. 1984. Role of the Fibula in
1226 Weight-bearing. *Clinical Orthopaedics and Related Research*® 184:289.
1227 Thermo Fisher Scientific. 2018. *Avizo*.

1228 Tougard C, Delefosse T, Hänni C, Montgelard C. 2001. Phylogenetic Relationships of the Five
1229 Extant Rhinoceros Species (Rhinocerotidae, Perissodactyla) Based on Mitochondrial
1230 Cytochrome b and 12S rRNA Genes. *Molecular Phylogenetics and Evolution* 19:34–44.
1231 DOI: 10.1006/mpev.2000.0903.
1232 Watson JC, Wilson AM. 2007. Muscle architecture of biceps brachii, triceps brachii and
1233 supraspinatus in the horse. *Journal of Anatomy* 210:32–40. DOI: 10.1111/j.1469-
1234 7580.2006.00669.x.
1235 Welker F, Smith GM, Hutson JM, Kindler L, Garcia-Moreno A, Villaluenga A, Turner E,
1236 Gaudzinski-Windheuser S. 2017. Middle Pleistocene protein sequences from the
1237 rhinoceros genus Stephanorhinus and the phylogeny of extant and extinct Middle/Late
1238 Pleistocene Rhinocerotidae. *PeerJ* 5:e3033. DOI: 10.7717/peerj.3033.
1239 Wiley DF, Amenta N, Alcantara DA, Ghosh D, Kil YJ, Delson E, Harcourt-Smith W, Rohlf FJ,
1240 St. John K, Hamann B. 2005. Evolutionary Morphing. In: *Proceedings of IEEE*
1241 *Visualization 2005*. Minneapolis, Minnesota,.
1242 Willerslev E, Gilbert MTP, Binladen J, Ho SY, Campos PF, Ratan A, Tomsho LP, da Fonseca
1243 RR, Sher A, Kuznetsova TV, Nowak-Kemp M, Roth TL, Miller W, Schuster SC. 2009.
1244 Analysis of complete mitochondrial genomes from extinct and extant rhinoceroses
1245 reveals lack of phylogenetic resolution. *BMC Evolutionary Biology* 9:95. DOI:
1246 10.1186/1471-2148-9-95.
1247 World Association of Veterinary Anatomists, International Committee on Veterinary Gross
1248 Anatomical Nomenclature. 2005. *Nomina anatomica veterinaria*. Hannover; Columbia
1249 [Mo.]; Ghent; Sapporo: The Editorial Committee.

1250 Zelditch ML, Swiderski DL, Sheets HD, Fink WL. 2012. *Geometric morphometrics for*
1251 *biologists: A Primer*. Academic Press.
1252 Zschokke S, Baur B. 2002. Inbreeding, outbreeding, infant growth, and size dimorphism in
1253 captive Indian rhinoceros (Rhinoceros unicornis). *Canadian Journal of Zoology* 80:2014–
1254 2023. DOI: 10.1139/z02-183.

Table 1(on next page)

Main characteristics of the five studied species

Length, height and body mass data compiled and calculated after (Dinerstein, 2011) . Ecological data compiled after (Becker, 2003) . **Abbreviations: G**: graviportal; **M**: mediportal. *: African species; **: Asiatic species

Species name	Length (cm)	Shoulder height (cm)	Mean body mass (kg)	Ecology	Locomotor type		
					(Gregory, 1912; Osborn, 1929; Coombs, 1978)	(Eisenmann & Guérin, 1984)	(Becker, 2003)
*Ceratotherium simum**	340 – 420	150 – 180	2,300	Open savanna	M	G	G
*Dicerorhinus sumatrensis***	236 – 318	100 – 150	775	Dense forests and swampy lakes	M	G	M
*Diceros bicornis**	300 – 380	140 – 170	1,050	Open savanna and clear forest	M	G	M
*Rhinoceros sondaicus***	305 – 344	150 – 170	1,350	Dense forests and swampy areas	M	G	G
*Rhinoceros unicornis***	335 – 346	175 – 200	2,000	Floodplains and swamps	M	G	M

1

Table 2(on next page)

List of the studied specimens with skeletal composition, sex, age class, condition and 3D acquisition details

Abbreviations: Bones – H: humerus; **R**: radius; **U**: ulna; **Fe**: femur; **T**: tibia; **Fi**: fibula. **Sex: F**: female; **M**: male; **U**: unknown. **Age – A**: adult; **Sa**: sub-adult. **Condition – W**: wild; **C**: captive; **U**: unknown. **3D acquisition – SS**: surface scanner; **P**: photogrammetry; **CT**: CT-scan. **Institutional codes: BICPC**: Powell Cotton Museum, Birchington-on-Sea. **CCEC**: Centre de Conservation et d'Étude des Collections, Musée des Confluences, Lyon. **MHNT:** Muséum d'Histoire Naturelle de Toulouse, Toulouse. **MNHN:** Muséum National d'Histoire Naturelle, Paris. **NHMUK:** Natural History Museum, London. **NHMW:** Naturhistorisches Museum Wien, Vienna. **NMS:** National Museums Scotland, Edinburgh. **RBINS:** Royal Belgian Institute of Natural Sciences, Brussels. **RMCA:** Royal Museum for Central Africa, Tervuren. **UCMP:** University of California Museum of Paleontology, Berkeley. **UMZC:** University Museum of Zoology Cambridge, Cambridge. **ZSM:** Zoologische Staatssammlung München, Munich. * Specimens NHMUK ZD 2018.143 and NHMUK ZD 1972.822 were determined by ourselves during the visit of the collections on the basis of morphological observations and measurements on the post-cranial elements. These determinations were later confirmed by our shape analysis. ** The specimen MNHN-ZM-AC-1885-734 was previously determined as *Rhinoceros sondaicus* based on a supposed Javan origin. The observations made on both long bones and tarsal elements led us to consider this individual as an Indian rhino (*Rhinoceros unicornis*). This attribution was later confirmed by our shape analysis

Taxon	Institution	Specimen number	H	R	U	Fe	T	Fi	Sex	Age	Condition	3D acquisition
*Ceratotherium simum**	NHMUK	ZD 2018.143	X	X	X	X	X	X	U	A	U	SS
Ceratotherium simum	NHMW	3086	X	X	X	X	X	X	U	A	W	P
Ceratotherium simum	RBINS	19904	X	X	X	X	X	X	M	S	W	SS
Ceratotherium simum	RBINS	35208	X	X	X	X		X	U	A	U	SS
Ceratotherium simum	RMCA	1985.32-M-0001	X	X	X	X	X	X	U	A	W	SS
Ceratotherium simum	RMCA	RG35146	X	X	X	X	X	X	M	A	W	SS
Ceratotherium simum	UCMP	125000				X			U	A	U	CT
Ceratotherium simum	ZSM	1912/4199				X			U	A	W	SS
Ceratotherium simum	BICPC	NH.CON.20	X	X	X	X	X	X	M	S	W	SS
Ceratotherium simum	BICPC	NH.CON.32	X	X	X	X	X	X	F	S	W	SS
Ceratotherium simum	BICPC	NH.CON.37	X	X		X	X	X	F	A	W	SS
Ceratotherium simum	BICPC	NH.CON.40	X	X	X	X	X	X	F	S	W	SS
Ceratotherium simum	BICPC	NH.CON.110	X	X	X	X	X	X	M	A	W	SS
Ceratotherium simum	BICPC	NH.CON.112	X	X	X	X	X	X	M	A	W	SS
Ceratotherium simum	NMS	NMS.Z.2010.44	X			X			F	A	U	CT
Ceratotherium simum	MNHN	ZM-MO-2005-297	X			X	X	X	M	A	C	SS
Dicerorhinus sumatrensis	MNHN	ZM-AC-1903-300	X	X	X	X	X	X	M	A	W	SS
Dicerorhinus sumatrensis	MNHN	ZM-AC-A7967	X	X	X				F	A	W	SS
Dicerorhinus sumatrensis	NHMUK	ZD 1879.6.14.2	X	X	X	X	X	X	M	A	W	SS
Dicerorhinus sumatrensis	NHMUK	ZD 1894.9.24.1	X	X	X	X	X	X	U	A	W	SS
Dicerorhinus sumatrensis	NHMUK	ZD 1931.5.28.1	X	X	X	X	X	X	M	S	W	SS
Dicerorhinus sumatrensis	NHMUK	ZE 1948.12.20.1	X	X	X	X	X	X	U	A	U	SS
Dicerorhinus sumatrensis	NHMUK	ZE 1949.1.11.1	X	X	X	X	X	X	U	A	W	SS
Dicerorhinus sumatrensis	NHMUK	ZD 2004.23	X			X	X	X	U	A	W	SS
Dicerorhinus sumatrensis	NHMW	1500				X	X	X	M	A	U	P
Dicerorhinus sumatrensis	NHMW	3082	X	X	X	X	X	X	U	A	U	P
Dicerorhinus sumatrensis	NHMW	29568		X	X	X		X	U	S	U	P
Dicerorhinus sumatrensis	RBINS	1204	X	X	X	X	X	X	M	A	W	SS
Dicerorhinus sumatrensis	UMZC	H.6392	X						U	A	U	CT
Dicerorhinus sumatrensis	ZSM	1908/571	X	X		X	X	X	M	A	U	SS
Diceros bicornis	CCEC	50002040	X			X	X	X	U	A	W	SS
Diceros bicornis	CCEC	50002044		X		X			U	S	U	SS
Diceros bicornis	CCEC	50002045				X			U	S	W	SS
Diceros bicornis	CCEC	50002046	X	X	X		X	X	U	S	U	SS
Diceros bicornis	CCEC	50002047		X	X		X	X	U	A	U	SS
Diceros bicornis	MNHN	ZM-AC-1936-644	X	X	X	X	X	X	F	S	U	SS
Diceros bicornis	MNHN	ZM-AC-1944-278	X			X	X	X	M	A	C	SS
Diceros bicornis	MNHN	ZM-AC-1974-124				X	X	X	F	A	C	SS
Diceros bicornis	RBINS	9714	X	X	X	X	X	X	F	A	W	SS
Diceros bicornis	RMCA	RG2133	X	X	X	X	X	X	M	S	W	SS
Diceros bicornis	UCMP	9856					X		U	A	U	CT
Diceros bicornis	ZSM	1961/186	X	X	X	X	X	X	M	S	U	SS
Diceros bicornis	ZSM	1961/187	X	X	X	X	X	X	M	S	U	SS

Diceros bicornis	ZSM	1962/166	X	X	X	X	X		F	S	U	SS
Rhinoceros sondaicus	CCEC	50002041	X	X	X	X	X	X	U	A	W	SS
Rhinoceros sondaicus	CCEC	50002043	X	X	X	X			U	A	W	SS
Rhinoceros sondaicus	MNHN	ZM-AC-A7970	X	X	X	X	X	X	U	A	U	SS
Rhinoceros sondaicus	MNHN	ZM-AC-A7971	X	X	X	X	X	X	U	A	W	SS
Rhinoceros sondaicus	NHMUK	ZD 1861.3.11.1	X	X	X	X	X	X	U	S	W	SS
Rhinoceros sondaicus	NHMUK	ZD 1871.12.29.7	X	X	X	X	X	X	M	A	W	SS
Rhinoceros sondaicus	NHMUK	ZD 1921.5.15.1	X	X	X	X	X	X	F	S	W	SS
Rhinoceros sondaicus	RBINS	1205F	X	X	X	X	X	X	U	S	W	SS
*Rhinoceros unicornis***	MNHN	ZM-AC-1885-734	X	X	X	X	X		U	A	W	SS
Rhinoceros unicornis	MNHN	ZM-AC-1932-49	X				X	X	U	S	U	SS
Rhinoceros unicornis	MNHN	ZM-AC-1960-59	X	X	X	X	X	X	M	A	C	SS
Rhinoceros unicornis	MNHN	ZM-AC-1967-101	X	X	X	X	X		F	A	C	SS
Rhinoceros unicornis	NHMUK	ZD 1884.1.22.1.2	X	X	X	X	X	X	F	A	W	SS
Rhinoceros unicornis	NHMUK	ZE 1950.10.18.5	X	X	X	X	X	X	M	A	W	SS
Rhinoceros unicornis	NHMUK	ZE 1961.5.10.1	X	X	X	X	X	X	M	A	W	SS
*Rhinoceros unicornis**	NHMUK	ZD 1972.822	X	X	X	X	X	X	U	A	U	SS
Rhinoceros unicornis	RBINS	1208	X	X	X	X	X	X	F	A	C	SS
Rhinoceros unicornis	RBINS	33382	X	X	X	X	X	X	U	A	U	SS

1

Table 3(on next page)

Results of the Pearson’s correlation tests between the log-transformed centroid size and the two first principal components for each bone

Significant results are indicated in bold.

1

2

Bone	Component	r	t	dF	P
Humerus	PC1	-0.38	-2.93	51	**0.01**
	PC2	0.43	3.44	51	**<0.01**
Radius	PC1	-0.64	-5.77	47	**<0.01**
	PC2	0.22	1.58	47	0.12
Ulna	PC1	-0.79	-8.44	44	**<0.01**
	PC2	0.02	0.11	44	0.91
Femur	PC1	-0.56	-5.01	54	**<0.01**
	PC2	0.30	-2.34	54	**0.02**
Tibia	PC1	-0.58	-5.05	51	**<0.01**
	PC2	0.08	0.58	51	0.57
Fibula	PC1	-0.36	-2.69	48	**<0.01**
	PC2	-0.34	-2.47	48	**0.02**
	PC3	0.16	1.12	48	0.27

Table 4(on next page)

Main anatomical differences observed between theoretical shapes associated with minimal and maximal centroid size for each bone of the forelimb

B: Bone; H: Humerus; R: Radius; U: Ulna.

B	Anatomical feature	Centroid size minimum	Centroid size maximum
H	General aspect	Slender	Robust
	Head	Rounded, overhanging the shaft	Rounded, overhanging poorly the shaft
	Lesser tubercle	Developed	Poorly developed
	Intermediate tubercle	Almost absent	Poorly developed
	Greater tubercle	Developed	Strongly developed
	Bicipital groove	Asymmetrical and closed	Almost symmetrical and widely open
	M. infraspinatus insertion	Diamond-shaped and strongly developed	Ovoid and less developed
	Deltoid tuberosity	Poorly laterally deviated and caudally sharp	Laterally deviated and caudally smooth
	Distal epiphysis	Medio-laterally compressed	Medio-laterally extended
	Supracondylar crest	Smooth	Very smooth
	Lateral epicondyle	Poorly extended laterally	Strongly extended laterally
	Medial epicondyle	Overhanging the olecranon fossa	Not overhanging the olecranon fossa
	Olecranon fossa	Triangular and deep	Rectangular and deep
	Trochlea	Sharp lips and deep groove	Smooth lips and shallow groove
	Capitulum	Extremely reduced	Extremely reduced
R	General aspect	Slender	Robust
	Proximal articular surface	Open and little concave; medial glenoid cavity slightly larger than the lateral one	Concave; medial glenoid cavity twice as large as the lateral one
	Radial tuberosity	Poorly developed	Poorly developed
	Lateral insertion relief	Poorly developed	Knob-shaped
	Lateral synovial articulation surface	Trapezoid and laterally extended	Trapezoid and laterally reduced
	Medial synovial articulation surface	Thin and rectangular	Thin and rectangular
	Proximal articular surface for the ulna	Triangular, wide and proximo-distally short	Triangular, slender and proximo-distally long
	Interosseous crest	Smooth	Sharp
	Interosseous space position	Mid-shaft	First proximal third of the shaft
	Distal articular surface for the ulna	Long and slender triangle	Short and wide triangle
	Articular surface for the carpal bones	Broad in dorso-palmar direction	Compressed in dorso-palmar direction

	Articular surface for the scaphoid	Proximally extended	Poorly extended proximally
	Articular surface for the semilunar	Trapezoid and narrow	Trapezoid and wide
	Radial styloid process	Short	Long
U	General aspect	Slender	Robust
	Olecranon	Medio-laterally compressed	Medio-laterally large
	Olecranon tuberosity	Oriented medially with a medial tubercle pointing in the medio-palmar direction	Oriented laterally with a medial tubercle pointing in the medio-dorsal direction
	Anconeus process	Developed in dorsal direction	Little developed dorsally
	Articular surface for the humerus	Medio-laterally reduced, lateral lip developed in proximal direction	Medio-laterally broad with an important development of the medial part
	Interosseous crest	Irregular and sharp	Smooth
	Distal epiphysis	Thin with a small lateral extension	Large and extending largely in lateral and dorsal directions
	Articular surface for the triquetrum	Narrow and concave	Wide and slightly concave
	Articular surface for the pisiform	Extended in proximal direction	Little developed in proximal direction

1

Table 5(on next page)

Main anatomical differences observed between theoretical shapes associated with minimal and maximal centroid size for each bone of the hind limb

B: Bone; Fe: Femur; Fi: Fibula; T: Tibia.

B	Anatomical feature	Centroid size minimum	Centroid size maximum
Fe	General aspect	Slender	Robust
	Head	Rounded, well separated from the shaft by a narrow neck	Massive and flattened, surmounting a large neck
	Fovea capitis	Formed by a simple shallow notch on the border head in medio-caudal direction	Small and shallow, oriented more medially
	Greater trochanter	Small and developed in the cranial direction	Large and developed in the latero-distal direction
	Lesser trochanter	Thin and bordering the caudal border of the shaft medial side	Thick, occupying the whole width of the medial side
	Lines on the cranial side	Medial line running straight along the side	Medial line strongly concave along the side
	Third trochanter	Rounded and poorly developed	Strong and developed towards the greater trochanter
	Trochlea	Oriented medially with a shallow groove and developed medial lip	Oriented cranially with a deep groove and an extremely developed medial lip
	Condyles	Almost of the same size	Medial condyle more developed than the lateral one
	Intercondylar space	Wide	Narrow
T	General aspect	Slender	Robust
	Proximal condyles	Nearly equal surface areas; lateral condyle more developed caudally with a sliding surface for the *m. popliteus*	Medial condyle surface twice as wide as the lateral one and more developed caudally
	Intercondylar tubercles	Nearly of equal height	Medial tubercle higher than the lateral one
	Central intercondylar area	Wide	Narrow
	Tibial tuberosity	Laterally deviated	Massive and oriented in lateral direction
	Tuberosity groove	Deep	Shallow
	Extensor sulcus	Shallow	Shallow
	Proximal articular surface for the fibula	Nail-shaped	Triangular
	Interosseous crest	Sharp	Smooth
	Distal articular surface for the fibula	Narrow and triangular	Wide and triangular
	Articular surface for the talus	Rectangular, slightly tilted laterally	Squared, slightly oriented medially
	Medial groove for	Deep and narrow	Deep and narrow

	the talus		
	Lateral groove for the talus	Shallow and wide	Shallow and wide
Fi	General aspect	Slender	Robust
	Head	Flat and large, oriented cranio-medially	Small and oriented cranially
	Proximal articular surface for the tibia	Nail-shaped	Triangular
	Shaft	Thin and slightly concave, with two sharp crests running along the lateral side	Broad and straight, with two smooth crests running along the lateral side
	Distal articular surface for the tibia	Triangular, narrow and long	Triangular, wide and short
	Lateral malleolus	Two well-developed tubercles caudally oriented and separated by a deep groove	Two flat tubercles laterally oriented, with the cranial one being more developed, and separated by a shallow groove
	Articular surface for the talus	Kidney-shaped, broad in proximo-distal direction	Triangular, proximo-distally compressed

1

Table 6(on next page)

Results of the Procrustes ANOVA performed on shape data and log-transformed centroid size (Cs.) taking into account species (Sp.) affiliation

Significant results are indicated in bold.

1

2

		R^2	F	Z	P (>F)
Humerus	Cs.	0.13	17.38	5.13	**0.001**
	Sp.	0.53	17.72	8.50	**0.001**
Radius	Cs.	0.18	15.72	5.74	**0.001**
	Sp.	0.32	7.07	8.83	**0.001**
Ulna	Cs.	0.16	12.94	6.19	**0.001**
	Sp.	0.36	7.31	9.27	**0.001**
Femur	Cs.	0.14	14.41	6.07	**0.001**
	Sp.	0.37	9.56	10.08	**0.001**
Tibia	Cs.	0.13	11.62	5.13	**0.001**
	Sp.	0.36	8.06	9.03	**0.001**
Fibula	Cs.	0.10	6.61	3.77	**0.001**
	Sp.	0.26	4.47	5.61	**0.001**

Table 7 (on next page)

Results of the Procrustes ANOVA performed on shape data and cube root of the mean body mass

Significant results are indicated in bold.

1

2

	R^2	F	Z	P (>F)
Humerus	0.33	25.664	5.73	**0.001**
Radius	0.29	18.77	6.06	**0.001**
Ulna	0.21	11.22	5.57	**0.001**
Femur	0.26	18.61	6.39	**0.001**
Tibia	0.18	11.16	5.50	**0.001**
Fibula	0.11	5.91	3.40	**0.001**

3

Figure 1

esults of the PCA performed on morphometric data of the humerus

A: distribution of the specimens along the two first axes of the PCA; B to I: theoretical shapes associated with the minimum and maximum values of PC1: caudal (B, C), lateral (D, E), proximal (F, G) and distal (H, I) views for PC1 minimum (B, D, F, H) and PC1 maximum (C, E, G, I). Abbreviations – **B.g.**: Bicipital groove; **C.**: Capitulum; **D.t.**: Deltoid tuberosity; **E.c.**: Epicondylar crest; **G.t.**: Greater tubercle; **G.t.c.**: Greater tubercle convexity; **H.**: Head; **I.t.**: Intermediate tubercle; **L.e.**: Lateral epicondyle; **L.l.b.**: Lateral lip border; **L.t.**: Lesser tubercle; **L.t.c.**: Lesser tubercle convexity; **M.e.**: Medial epicondyle; ***M.i.*i.**: *M. infraspinatus* insertion; **M.l.b.**: Medial lip border; ***M.t.m.*t.**: *M. teres major* tuberosity; **N.**: Neck; **O.f.**: Olecranon fossa; **T.**: Trochlea; **T.g.**: Trochlear groove.

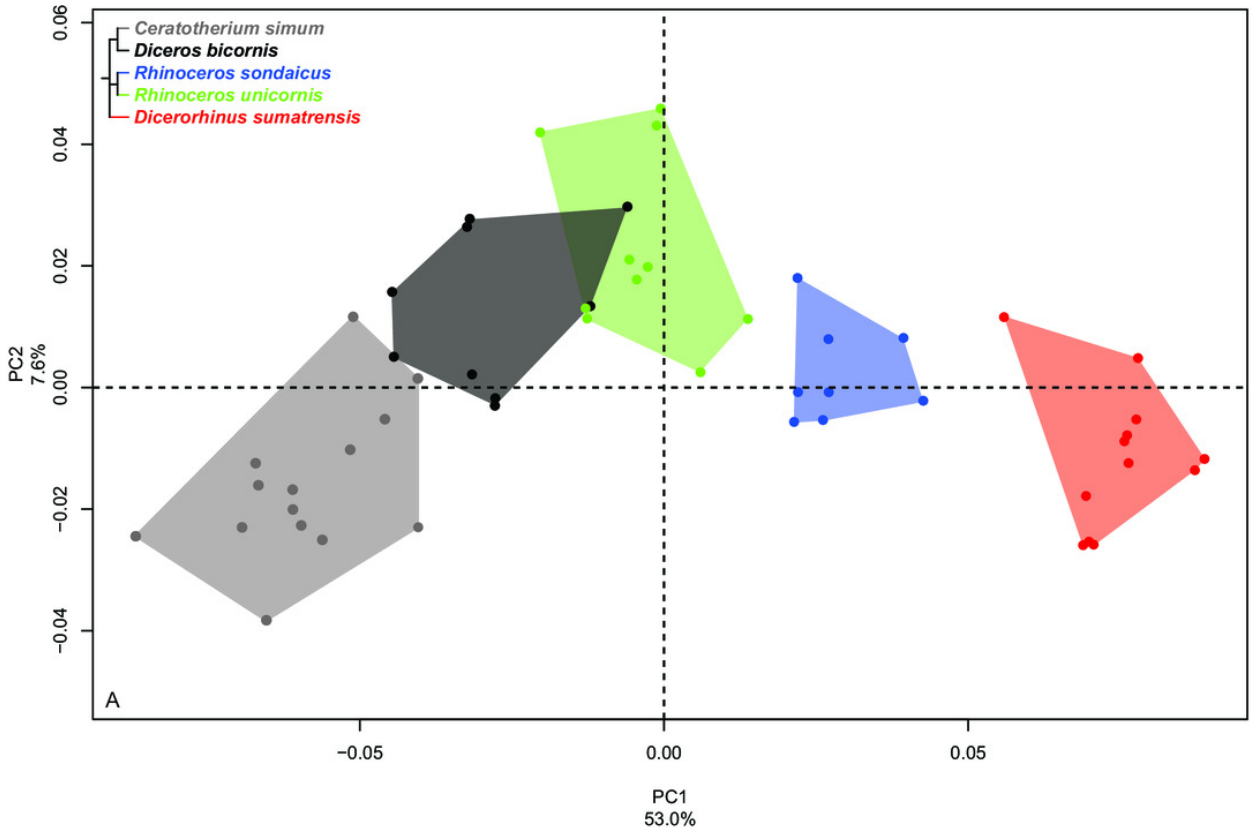
Ceratotherium simum
Diceros bicornis
Rhinoceros sondaicus
Rhinoceros unicornis
Dicerorhinus sumatrensis
PC2
7.6%
PC1
53.0%
0.06
0.04
0.02
0.00
−0.02
−0.04
−0.05
0.00
0.05
A

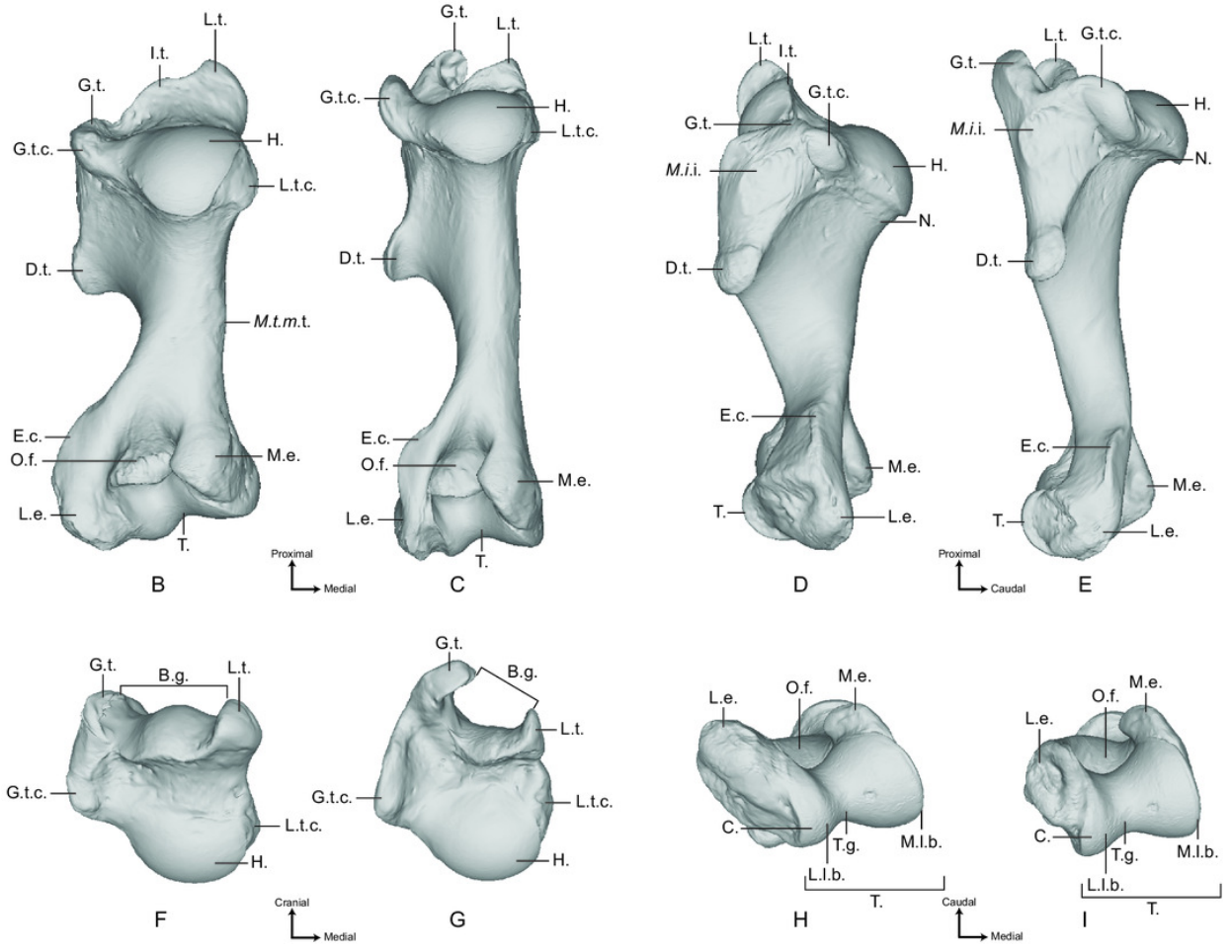
L.t.
I.t.
G.t.
G.t.c.
H.
L.t.c.
D.t.
M.t.m.t.
E.c.
O.f.
M.e.
L.e.
T.
Proximal
Medial
B
C
M.i.i.
N.
Caudal
D
E
B.g.
Cranial
F
G
C.
T.g.
M.l.b.
L.l.b.
H
I

Figure 2

Results of the PCA performed on morphometric data of the radius

A: distribution of the specimens along the two first axes of the PCA; B to I: theoretical shapes associated with the minimum and maximum values of PC1: dorsal (B, C), palmar (D, E), proximal (F, G) and distal (H, I) views for PC1 minimum (B, D, F, H) and PC1 maximum (C, E, G, I). Abbreviations – **A.s.s.**: Articular surface for the scaphoid; **A.s.sl.**: Articular surface for the semilunar; **C.p.**: Coronoid process; **D.a.s.u.**: Distal articular surface for the ulna; **I.c.**: Interosseous crest; **I.s.**: Interosseous space; **L.g.c.**: Lateral glenoid cavity; **L.i.r.**: Lateral insertion relief; **L.s.a.s.**: Lateral synovial articular surface; **M.g.c.**: Medial glenoid cavity; **M.s.a.s.**: Medial synovial articular surface; **P.a.s.u.**: Proximal articular surface for the ulna; **P.p.**: Palmar process; **R.s.p.**: Radial styloid process; **R.t.**: Radial tuberosity.

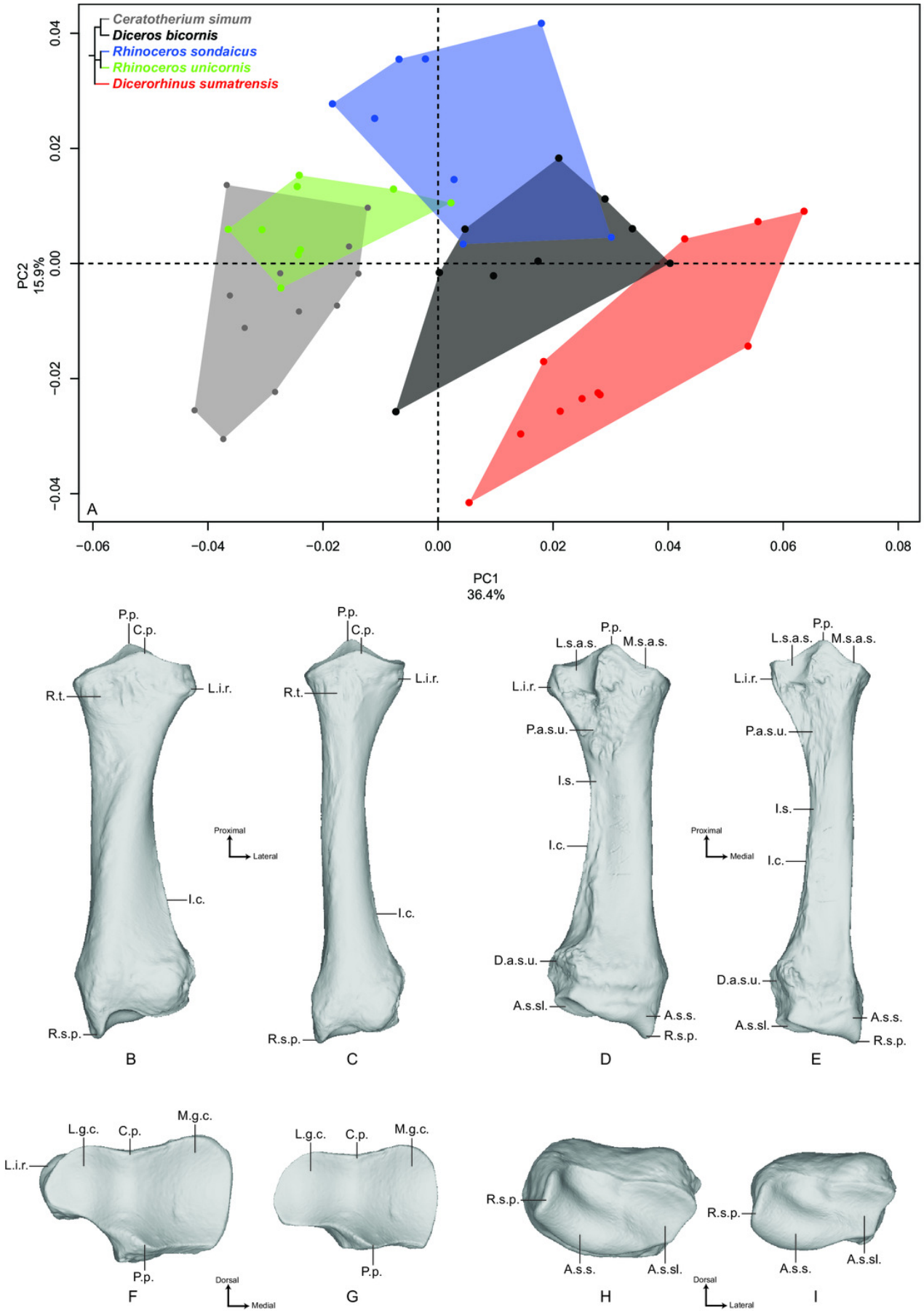
Ceratotherium simum
Diceros bicornis
Rhinoceros sondaicus
Rhinoceros unicornis
Dicerorhinus sumatrensis
PC2
15.9%
PC1
36.4%
A
B
C
D
E
F
G
H
I
P.p.
C.p.
L.i.r.
R.t.
I.c.
R.s.p.
L.s.a.s.
M.s.a.s.
P.a.s.u.
I.s.
D.a.s.u.
A.s.sl.
A.s.s.
L.g.c.
M.g.c.
Proximal
Lateral
Medial
Dorsal

Figure 3

Results of the PCA performed on morphometric data of the ulna

A: distribution of the specimens along the two first axes of the PCA; B to I: theoretical shapes associated with the minimum and maximum values of PC1: dorsal (B, C), medial (D, E), proximal (F, G) and distal (H, I) views for PC1 minimum (B, D, F, H) and PC1 maximum (C, E, G, I). Abbreviations – **A.p.**: Anconeus process; **A.s.h.**: Articular surface for the humerus; **A.s.p.**: Articular surface for the pisiform; **A.s.sl.**: Articular surface for the semilunar; **A.s.t.**: Articular surface for the triquetrum; **D.a.s.r.**: Distal articular surface for the radius; **I.c.**: Interosseous crest; **I.s.**: Interosseous space; **M.t.o.**: Medial tuberosity of the olecranon; **O.t.**: Olecranon tuberosity; **P.b.**: palmar border; **U.s.p.**: Ulnar styloid process.

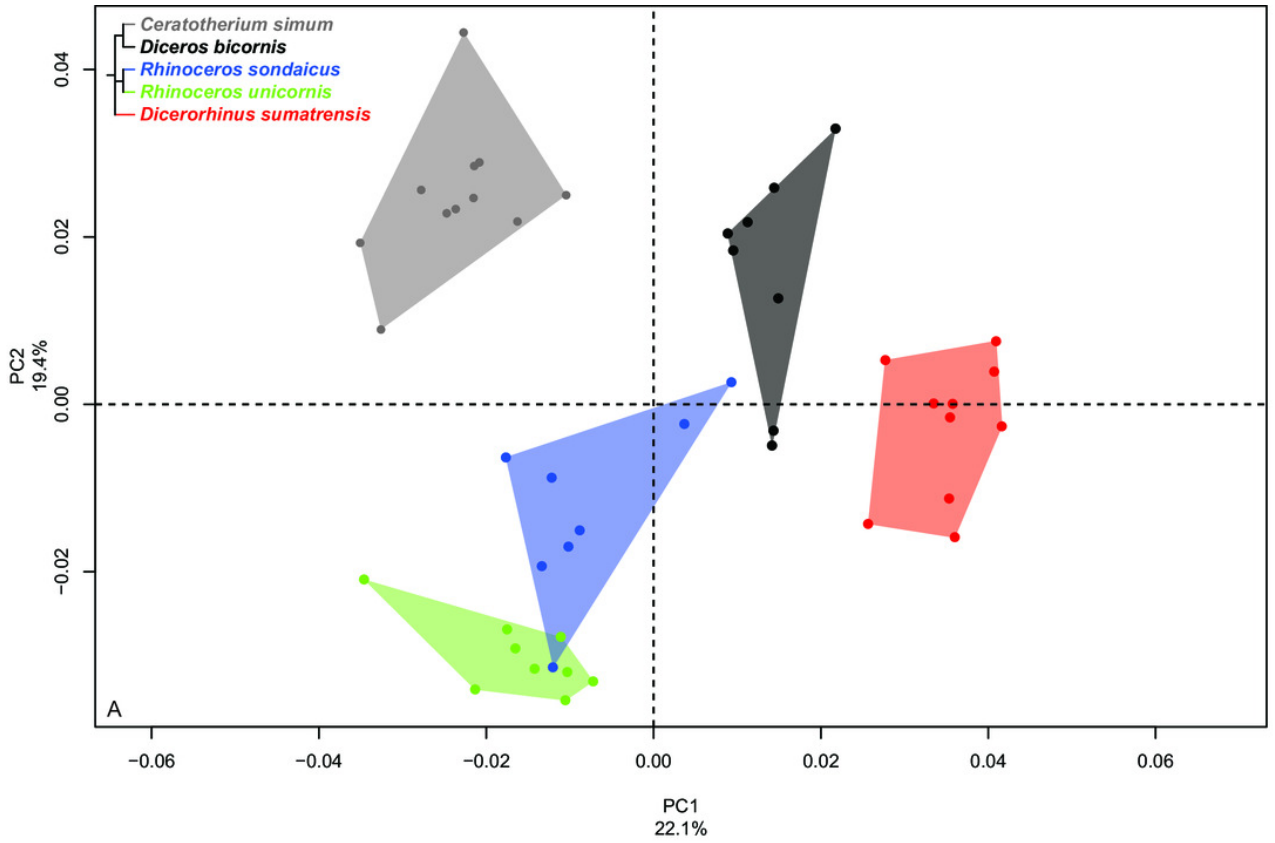
Ceratotherium simum
Diceros bicornis
Rhinoceros sondaicus
Rhinoceros unicornis
Dicerorhinus sumatrensis
PC2
19.4%
PC1
22.1%
0.04
0.02
0.00
−0.02
−0.06
−0.04
−0.02
0.00
0.02
0.04
0.06
A

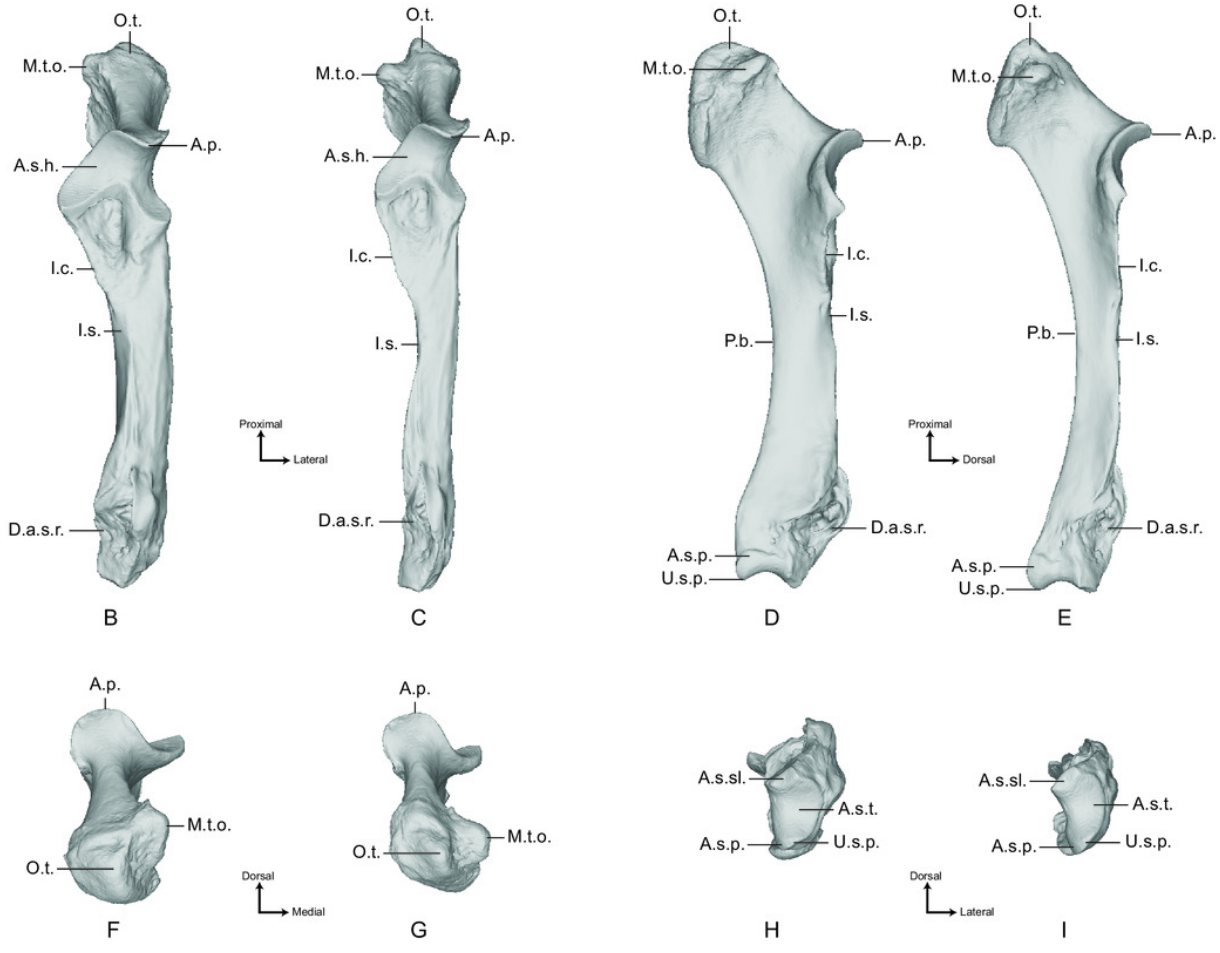
O.t.
M.t.o.
A.p.
A.s.h.
I.c.
I.s.
D.a.s.r.
Proximal
Lateral
B
C
P.b.
A.s.p.
U.s.p.
Dorsal
D
E
F
G
A.s.sl.
A.s.t.
Medial
H
I

Figure 4

Results of the PCA performed on morphometric data of the femur

A: distribution of the specimens along the two first axes of the PCA; B to I: theoretical shapes associated with the minimum and maximum values of PC1: cranial (B, C), medial (D, E), proximal (F, G) and distal (H, I) views for PC1 minimum (B, D, F, H) and PC1 maximum (C, E, G, I). Abbreviations – ***F.c.***: *Fovea capitis*; **G.t.**: Greater trochanter; **G.t.c.**: Greater trochanter convexity; **G.t.t.**: Greater trochanter top; **H.**: Head; **I.s.**: Intercondylar space; **L.c.**: Lateral condyle; **L.e.**: Lateral epicondyle; **L.l.**: Lateral lip; **L.t.**: Lesser trochanter; **M.c.**: Medial condyle; **M.e.**: Medial epicondyle; **M.l.**: Medial lip; **N.**: Neck; **S.f.**: supracondylar fossa; **T.**: Trochlea; **T.f.**: Trochanteric fossa; **T.g.**: Trochlear groove; **T.t.**: Third trochanter.

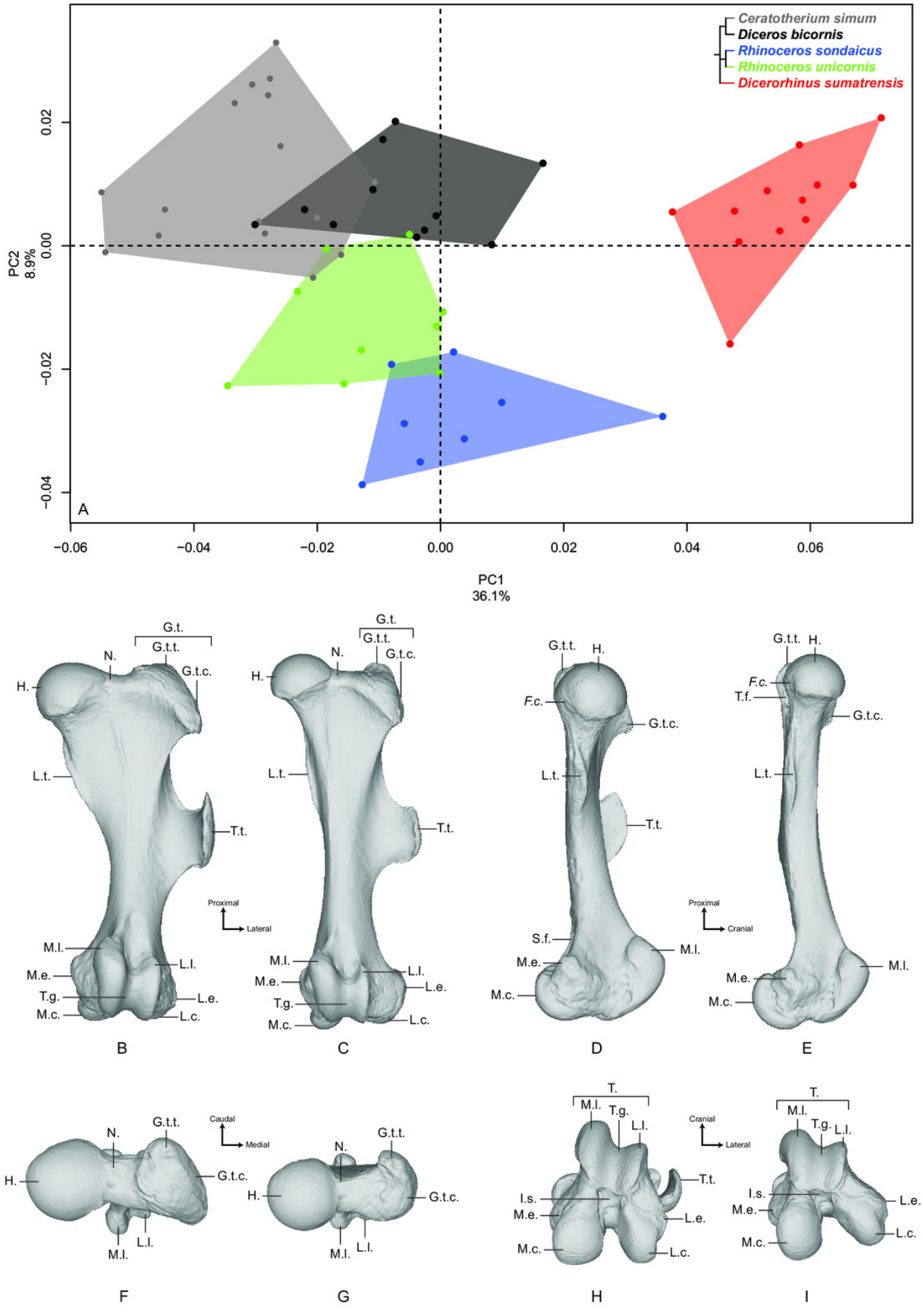
Ceratotherium simum
Diceros bicornis
Rhinoceros sondaicus
Rhinoceros unicornis
Dicerorhinus sumatrensis
PC2
8.9%
PC1
36.1%
A
B
C
D
E
F
G
H
I
G.t.
G.t.t.
G.t.c.
N.
H.
L.t.
T.t.
M.l.
L.l.
M.e.
T.g.
L.e.
M.c.
L.c.
F.c.
S.f.
T.f.
T.
I.s.
Proximal
Lateral
Cranial
Caudal
Medial

Figure 5

Results of the PCA performed on morphometric data of the tibia

A: distribution of the specimens along the two first axes of the PCA; B to I: theoretical shapes associated with the minimum and maximum values of PC1: cranial (B, C), lateral (D, E), proximal (F, G) and distal (H, I) views for PC1 minimum (B, D, F, H) and PC1 maximum (C, E, G, I). Abbreviations – **A.s.t.**: Articular surface for the talus; **C.a.**: Caudal apophysis; **Ce.i.a.**: Central intercondylar area; **Cr.i.a.**: Cranial intercondylar area; **D.a.s.f.**: Distal articular surface for the fibula; **E.g.**: Extensor groove; **I.c.**: Interosseous crest; **L.a.s.**: Lateral articular surface; **L.c.**: Lateral condyle; **L.g.**: Lateral groove; **L.i.t.**: Lateral intercondylar tubercle; **M.a.s.**: Medial articular surface; **M.c.**: Medial condyle; **M.g.**: Medial groove; **M.i.t.**: Medial intercondylar tubercle; **M.m.**: Medial malleolus; **P.a.s.f.**: Proximal articular surface for the fibula; **P.n.**: Popliteal notch; **S.s.*m.p.***: Sliding surface for the *m. popliteus*; **T.c.**: Tibial crest; **T.g.**: Tuberosity groove; **T.t.**: Tibial tuberosity.

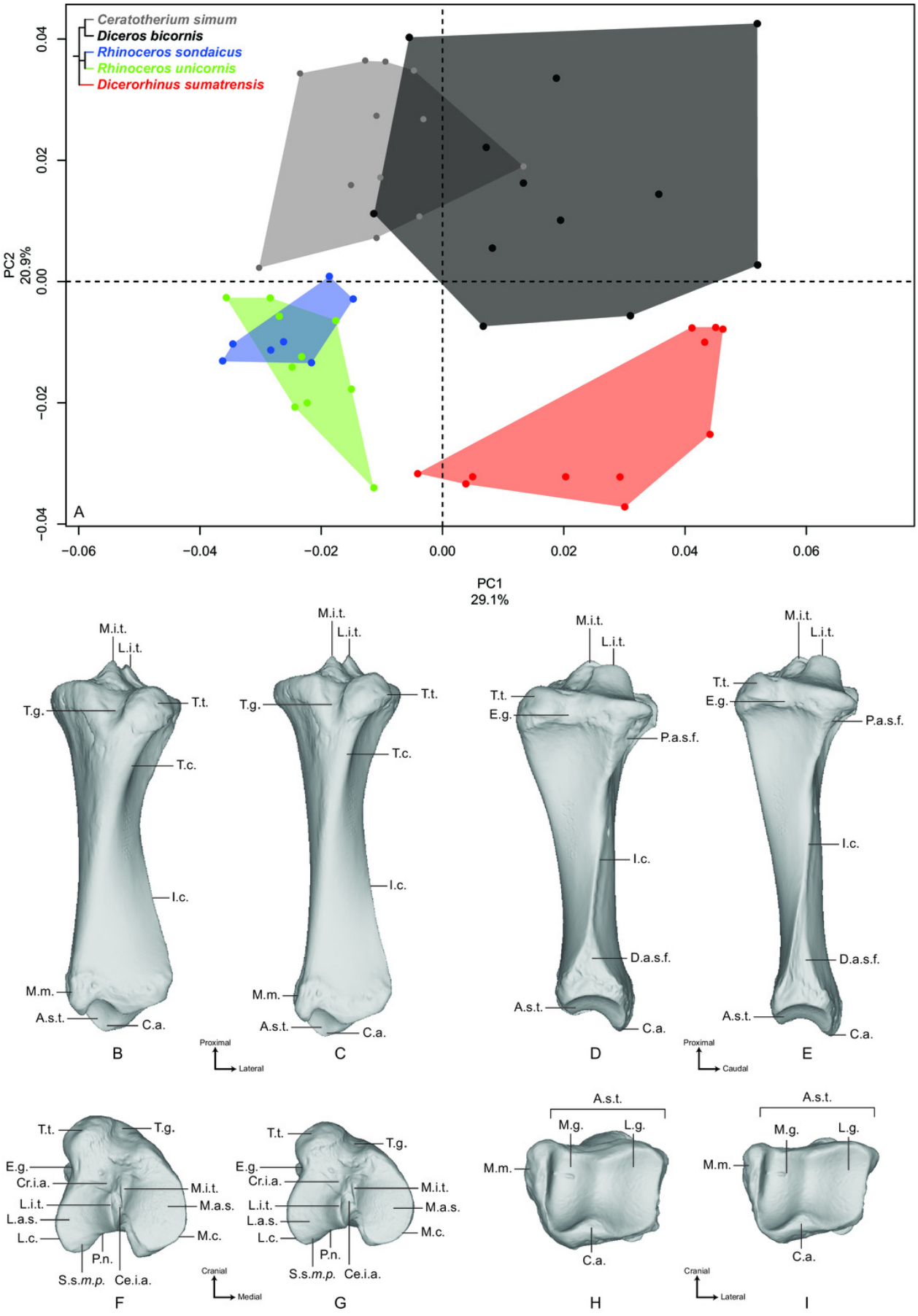
Ceratotherium simum
Diceros bicornis
Rhinoceros sondaicus
Rhinoceros unicornis
Dicerorhinus sumatrensis
A
PC2
20.9%
PC1
29.1%
0.04
0.02
0.00
−0.02
−0.04
−0.06
−0.04
−0.02
0.00
0.02
0.04
0.06
M.i.t.
L.i.t.
T.g.
T.t.
T.c.
I.c.
M.m.
A.s.t.
C.a.
B
C
D
E
Proximal
Lateral
Caudal
E.g.
P.a.s.f.
D.a.s.f.
T.t.
T.g.
E.g.
Cr.i.a.
M.i.t.
L.i.t.
M.a.s.
L.a.s.
L.c.
M.c.
P.n.
S.s.m.p.
Ce.i.a.
F
G
Cranial
Medial
A.s.t.
M.g.
L.g.
M.m.
C.a.
H
I
Lateral

Figure 6

Results of the PCA performed on morphometric data of the fibula

Distribution of the specimens along the two first axes of the PCA, taking into account the age class and the sex of each specimen. **Square**: female; **Triangle**: male; **Circle**: unknown; **Empty symbol**: subadult; **Filled symbol**: adult.

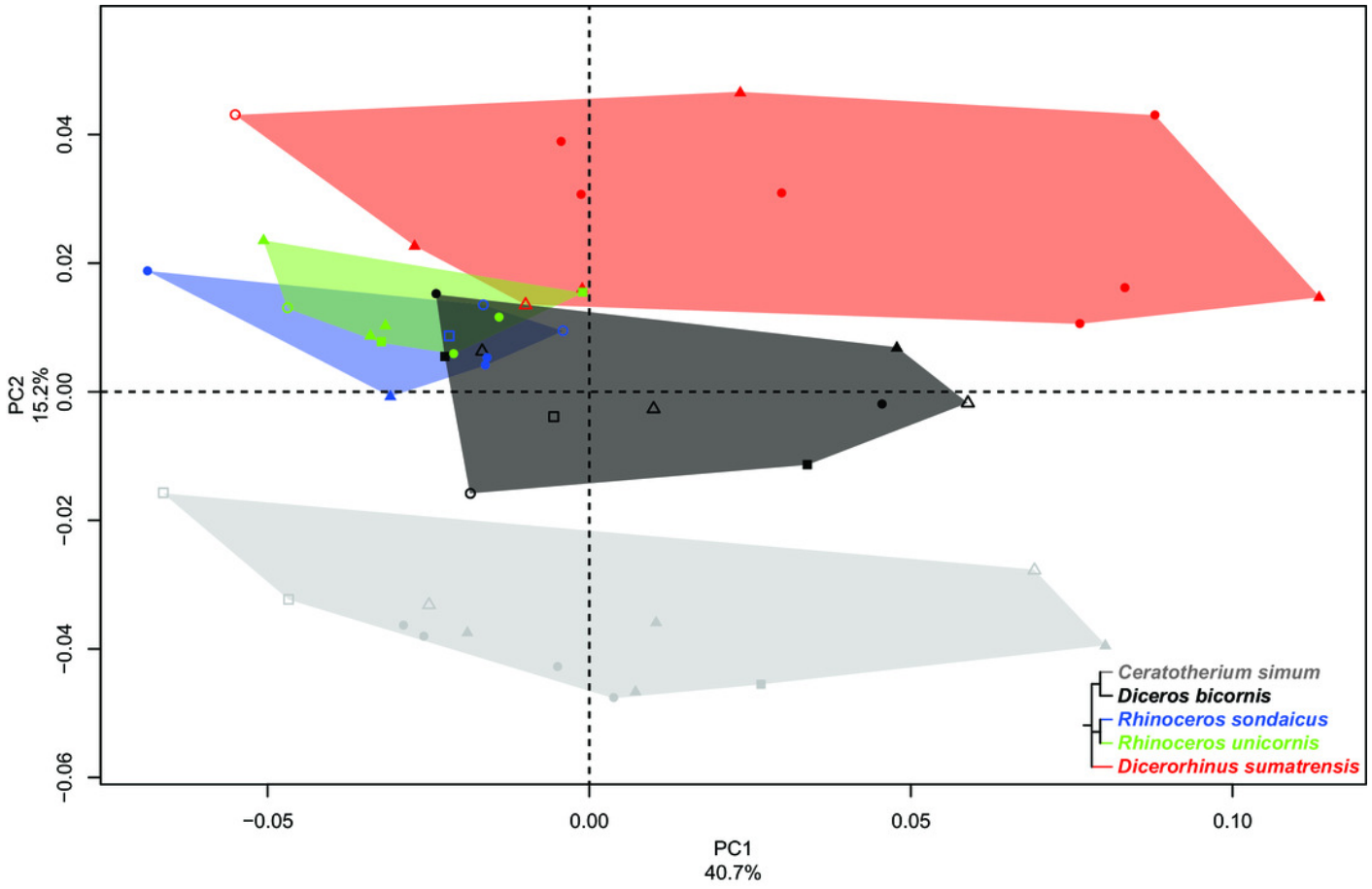

Figure 7

Results of the PCA performed on morphometric data of the fibula (second and third axes)

A: distribution of the specimens along the second and third axes of the PCA; B to K: theoretical shapes associated with the minimum and maximum values of PC2: lateral (B, C), cranial (D, E), medial (F, G), proximal (H, I) and distal (J, K) views for PC2 minimum (B, D, F, H, J) and PC2 maximum (C, E, G, I, K). Abbreviations – **A.s.t.**: Articular surface for the talus; **Ca.l.**: Caudo-lateral line; **Ca.t.l.m.**: Caudal tubercle of the lateral malleolus; **Cr.l.**: Cranio-lateral line; **Cr.t.l.m.**: Cranial tubercle of the lateral malleolus; **D.a.s.t.**: Distal articular surface for the tibia; **D.g.m.**: Distal groove of the malleolus; **H.**: Head; **I.c.**: Interosseous crest; **L.g.**: Lateral groove; **P.a.s.t.**: Proximal articular surface for the tibia.

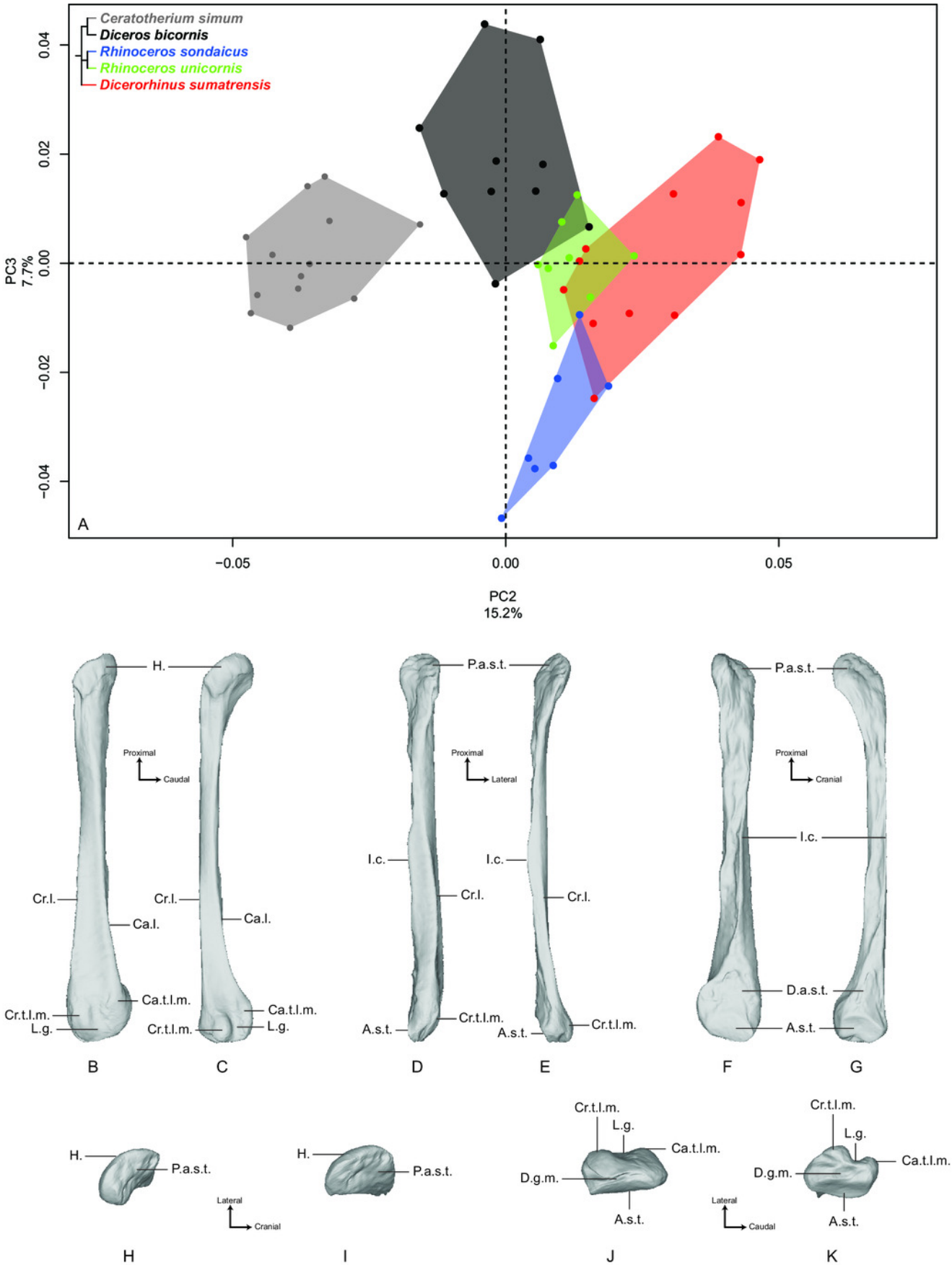
Ceratotherium simum
Diceros bicornis
Rhinoceros sondaicus
Rhinoceros unicornis
Dicerorhinus sumatrensis
PC3
7.7%
PC2
15.2%
A
B
C
D
E
F
G
H
I
J
K
H.
P.a.s.t.
Proximal
Caudal
Lateral
Cranial
Cr.l.
Ca.l.
Ca.t.l.m.
Cr.t.l.m.
L.g.
I.c.
A.s.t.
D.a.s.t.
D.g.m.

Figure 8

Landmark conformations associated to minimal and maximal centroid size and mean mass for each bone

A, B: Humerus (caudal view); C, D: Radius (dorsal view); E, F: Ulna (dorsal view); G, H: Femur (cranial view); I, J: Tibia (cranial view); K, L: Fibula (lateral view). **Red dots**: landmark conformation associated to the mean mass. **Blue dots**: landmark conformation associated to the centroid size. A, C, E, G, I, K: landmark conformation associated to the minimum of both parameters; B, D, F, H, J, L: landmark conformation associated to the maximum of both parameters.

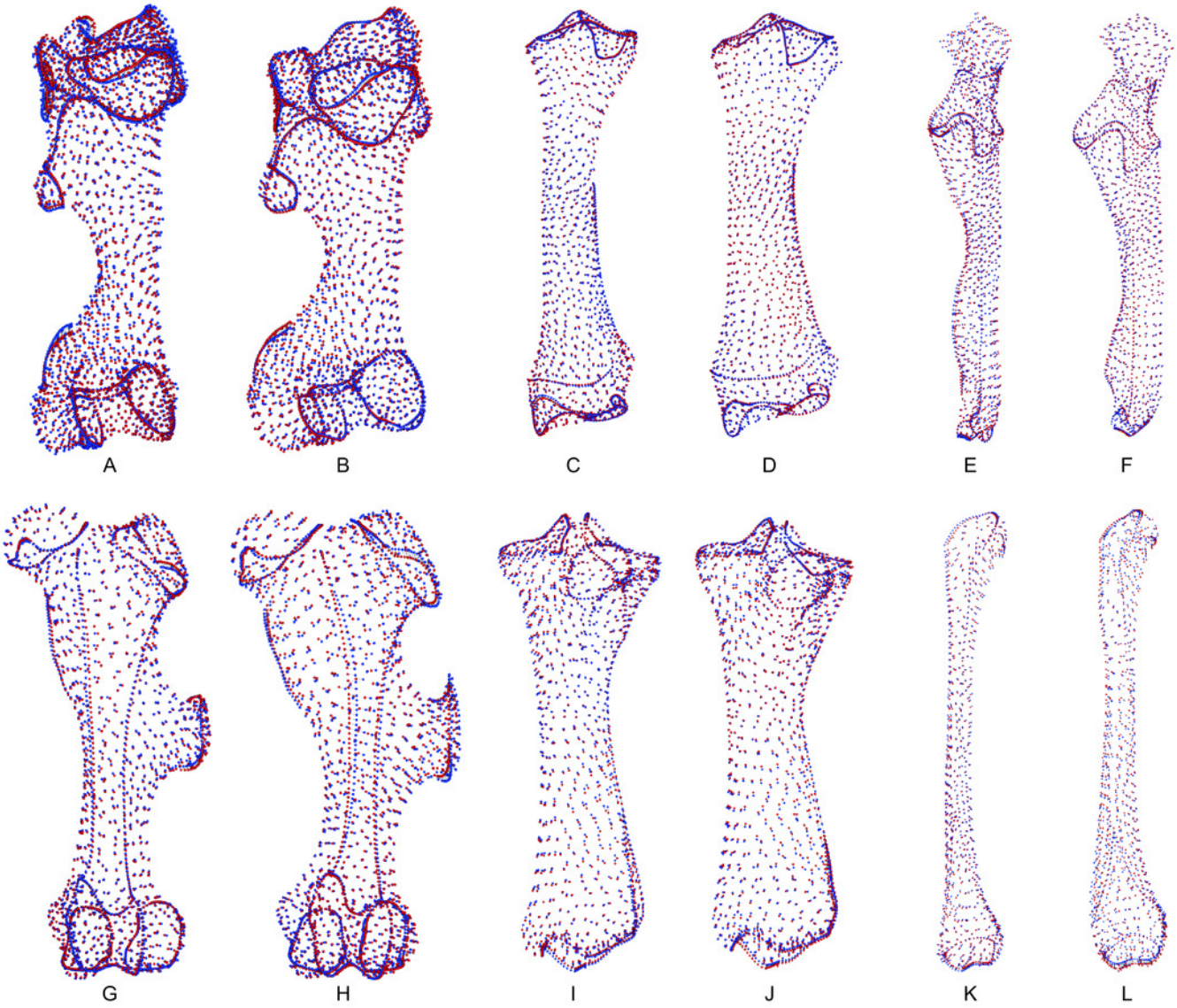
A
B
C
D
E
F
G
H
I
J
K
L

Figure 9

Multivariate regression plots performed on shape data and log-transformed centroid size

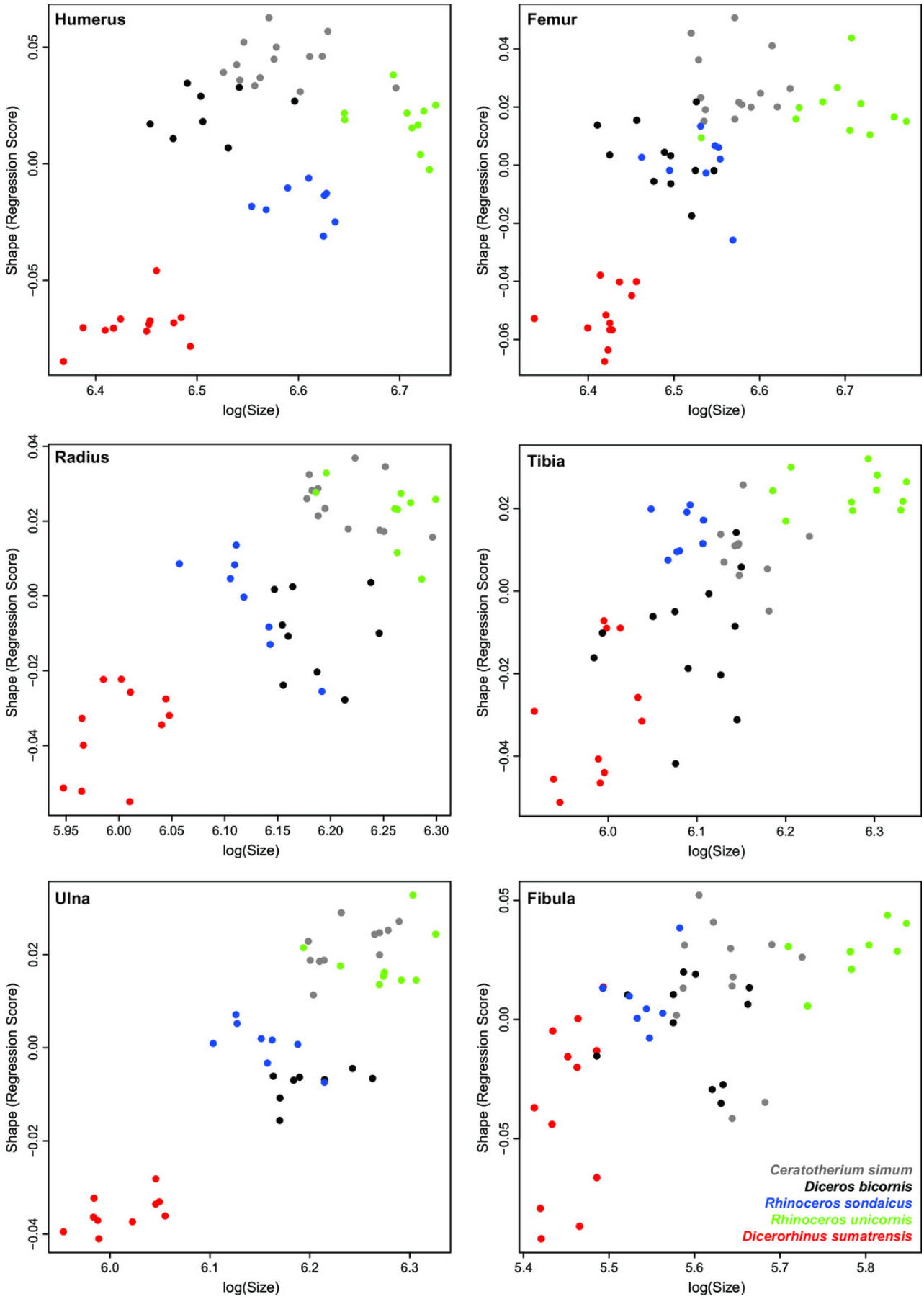
Humerus
Femur
Radius
Tibia
Ulna
Fibula
Shape (Regression Score)
log(Size)
Ceratotherium simum
Diceros bicornis
Rhinoceros sondaicus
Rhinoceros unicornis
Dicerorhinus sumatrensis